Clustering of Ca^{2+} transients in interstitial cells of Cajal defines slow wave duration

Bernard T. Drumm,* Grant W. Hennig,* Matthew J. Battersby, Erin K. Cunningham, Tae Sik Sung, Sean M. Ward, Kenton M. Sanders, and Salah A. Baker

Department of Physiology and Cell Biology, University of Nevada School of Medicine, Reno, NV

Interstitial cells of Cajal (ICC) in the myenteric plexus region (ICC-MY) of the small intestine are pacemakers that generate rhythmic depolarizations known as slow waves. Slow waves depend on activation of Ca^{2+}-activated Cl$^-$ channels (ANO1) in ICC, propagate actively within networks of ICC-MY, and conduct to smooth muscle cells where they generate action potentials and phasic contractions. Thus, mechanisms of Ca^{2+} regulation in ICC are fundamental to the motor patterns of the bowel. Here, we characterize the nature of Ca^{2+} transients in ICC-MY within intact muscles, using mice expressing a genetically encoded Ca^{2+} sensor, GCaMP3, in ICC. Ca^{2+} transients in ICC-MY display a complex firing pattern caused by localized Ca^{2+} release events arising from multiple sites in cell somata and processes. Ca^{2+} transients are clustered within the time course of slow waves but fire asynchronously during these clusters. The durations of Ca^{2+} transient clusters (CTCs) correspond to slow wave durations (plateau phase). Simultaneous imaging and intracellular electrical recordings revealed that the upstroke depolarization of slow waves precedes clusters of Ca^{2+} transients. Summation of CTCs results in relatively uniform Ca^{2+} responses from one slow wave to another. These Ca^{2+} transients are caused by Ca^{2+} release from intracellular stores and depend on ryanodine receptors as well as amplification from IP$_3$ receptors. Reduced extracellular Ca^{2+} concentrations and T-type Ca^{2+} channel blockers decreased the number of firing sites and firing probability of Ca^{2+} transients. In summary, the fundamental electrical events of small intestinal muscles generated by ICC-MY depend on asynchronous firing of Ca^{2+} transients from multiple intracellular release sites. These events are organized into clusters by Ca^{2+} influx through T-type Ca^{2+} channels to sustain activation of ANO1 channels and generate the plateau phase of slow waves.

INTRODUCTION

Phasic contractions of gastrointestinal (GI) muscles are the basis for gastric peristalsis and segmental contractions in the intestine and depend on rhythmic electrical depolarization events known as slow waves (Burnstock et al., 1963). Interstitial cells of Cajal (ICC) are the pacemaker cells that generate slow waves in the GI tract (Langton et al., 1989; Ward et al., 1994; Huizinga et al., 1995; Torihashi et al., 1995; Dickens et al., 1999; Sanders et al., 2014). There are several classes of ICC in GI muscles, and there are important differences in their ability to generate pacemaker activity and electrical slow waves. In the stomach and small intestine, ICC that lie in the plane of the myenteric plexus (ICC-MY) are pacemaker cells (Ward et al., 1994; Dickens et al., 1999; Ördög et al., 1999), whereas the cells in muscular bundles (ICC-IM and ICC-DMP in the small intestine) are involved in neurotransmission and responses to stretch (Burns et al., 1996; Ward et al., 2000; Won et al., 2005). Both of these ICC types generate Ca^{2+} transients and spontaneous transient inward currents (STICs) that result from activation of a Ca^{2+}-activated Cl$^-$ conductance

(Zhu et al., 2011), but ICC-MY also possess a voltage-dependent mechanism that allows depolarization-dependent activation of slow wave currents (Hirst et al., 2002; Zhu et al., 2009). The mechanism for the voltage-dependent element is controversial, and voltage-dependent enhancement in inositol tri-phosphate (IP$_3$) production and voltage-dependent entry of Ca^{2+} have been suggested (Hirst et al., 2002; Park et al., 2006; Zheng et al., 2014). Freshly dispersed ICC from the small intestine express T-type Ca^{2+} channels (*Cacna1h*) and a T-like, voltage-dependent Ca^{2+} conductance (Zheng et al., 2014). Voltage-dependent IP$_3$ production has never been demonstrated in ICC.

Pacemaker activity results from STICs that then initiate coordinated activation of Ca^{2+}-activated Cl$^-$ channels that summate to cause the depolarization responses known as slow waves (Hirst et al., 2002; Kito et al., 2005, 2015). *Ano1* encodes the Ca^{2+}-activated Cl$^-$ channels responsible for STICs and slow waves in ICC, and knockout of this gene renders gastric and small intestinal muscles devoid of slow wave activity (Hwang et al., 2009; Zhu et al., 2009; Singh et al., 2014). Ano1 channels are

---

voltage independent, and therefore a rise in intracellular Ca^{2+} is necessary for STICs and ultimately slow waves (Hwang et al., 2009; Zhu et al., 2009, 2015). Loading muscles with membrane-permeable Ca^{2+} chelators can inhibit slow waves, and several previous studies have shown that a variety of Ca^{2+} store–active drugs can affect the occurrence and frequency of slow waves (Malysz et al., 2001; Ward et al., 2003; Bayguinov et al., 2007; Kito et al., 2015). Previous studies using tissues loaded with Fluo-4 have documented Ca^{2+} waves spreading through ICC-MY networks, and these events were associated with slow wave activity (Park et al., 2006; Lee et al., 2007; Lowie et al., 2011; Singh et al., 2014), but there is much to learn about the dynamics and sources of Ca^{2+} that initiate cellular Ca^{2+} transients in ICC. For example, the release of Ca^{2+} and its activating effects on Ano1 channels may be highly localized within microdomains that tightly control local $[Ca^{2+}]$, because dialysis of ICC with Ca^{2+} concentrations of up to 2 µM fails to activate Cl^- current (Zhu et al., 2015).

Slow waves were so termed because of their relatively long duration (>1 s), as compared with the brief depolarization events (action potentials) in most excitable cells. In the small intestine, the plateau phase of slow waves provides depolarization sufficient to activate voltage-dependent Ca^{2+} channels in smooth muscle cells that are the major signal for initiation of excitation-contraction coupling (Langton et al., 1989; Ozaki et al., 1991). The duration and amplitude of slow waves therefore largely determines the force of contractions and the characteristics of intestinal motor activity. However, a major deficit in our knowledge is why the plateau potential of slow waves is sustained for more than a second in the small intestine and up to many seconds in some other GI muscles (Sanders et al., 2014). The plateau phase, largely the result of the rise of Cl^- permeability caused by activation of Ano1 channels, persists at or near the equilibrium potential for the transmembrane Cl^- gradient (E_{Cl}), suggesting that a mechanism to sustain $[Ca^{2+}]$ near the cytoplasmic aspect of Ano1 channels exists (Zhu et al., 2009). Ca^{2+} transients resulting from release of Ca^{2+} from stores are typically brief, as stores are unloaded and must be refilled or ER Ca^{2+} release channels must recover from a refractory period before another release event occurs (Bootman et al., 2001). Regulation of pacemaker activity and the amplitude and duration of slow waves are important topics because several GI motility disorders have been associated with defects and/or loss of ICC (Ördög et al., 2000; Iwasaki et al., 2001; Yamamoto et al., 2008; Wang et al., 2009). It is possible that well before the disappearance of these cells, defects in Ca^{2+} signaling and pacemaker activity initiate functional abnormalities in GI motility.

In the present study, we used animals expressing the genetically encoded Ca^{2+} sensor, GCaMP3, to investigate subcellular Ca^{2+} signaling in ICC-MY networks in situ during propagated slow waves in the murine small intestine. We hypothesized that propagation of pacemaker activity through ICC-MY networks must initiate a sustained source of Ca^{2+} that might be caused by periodic, but asynchronous, release of Ca^{2+} from intracellular stores distributed throughout the network. We sought to determine whether Ca^{2+} release occurs in both the somata and processes of ICC-MY and whether the behavior and excitability (i.e., probability of Ca^{2+} release) of Ca^{2+} release sites differ in these subcellular regions. We also tested whether Ca^{2+} release events in ICC-MY are triggered by Ca^{2+} entry through a voltage-dependent Ca^{2+} conductance that might serve as the basis for propagation of slow waves in GI muscles.

MATERIALS AND METHODS

Animals
The animals used and the experiments performed in this study were in accordance with the National Institutes of Health Guide for the Care and Use of Laboratory Animals. All procedures were approved by the Institutional Animal Use and Care Committee at the University of Nevada, Reno. GCaMP3-floxed mice (B6.129S-*Gt(RO-SA)26Sor*$^{tm38(CAG-GCaMP3)Hze}$/J) and associated wild-type siblings (C57BL/6) were purchased from The Jackson Laboratory. Kit-Cre mice (c-Kit$^{+/Cre-ERT2}$) were gifted from D. Saur (Technical University Munich, Munich, Germany). Once crossed, these mice (Kit-Cre-GCaMP3) were injected with tamoxifen at 6–8 wk of age (2 mg for three consecutive days) as described previously (Baker et al., 2016) to induce cre recombinase activation and subsequent GCaMP3 expression and were anaesthetized by inhalation with isoflurane (Baxter) and killed by cervical dislocation 50 d later.

Tissue preparation
Segments of jejunum 2 cm in length were removed from mice after an abdominal incision and bathed in Krebs-Ringer bicarbonate solution (KRB). The tissues were opened along the mesenteric border, and intra-luminal contents were washed away with cold KRB. The mucosa and sub-mucosa layers were then removed by sharp dissection and tissues were pinned flat in a Sylgard coated dish with the serosal side of the muscles facing the bottom of the dish.

Drugs and solutions
All tissues were perfused and maintained with KRB solution containing (mmol/liter): 120.35 NaCl, 15.5 $NaHCO_3$, 5.9 KCl, 1.2 $MgCl_2$, 1.2 NaH_2PO_4, 2.5 $CaCl_2$, and 11.5 glucose. The KRB solution warmed to a physiological temperature of 37 ± 0.2°C and bubbled with a mixture of 97% O_2–3% CO_2. For experiments using external solutions with zero $[Ca^{2+}]_o$, $CaCl_2$ was omitted and 1 mM EGTA was added to the solution. NNC 55-0396 and
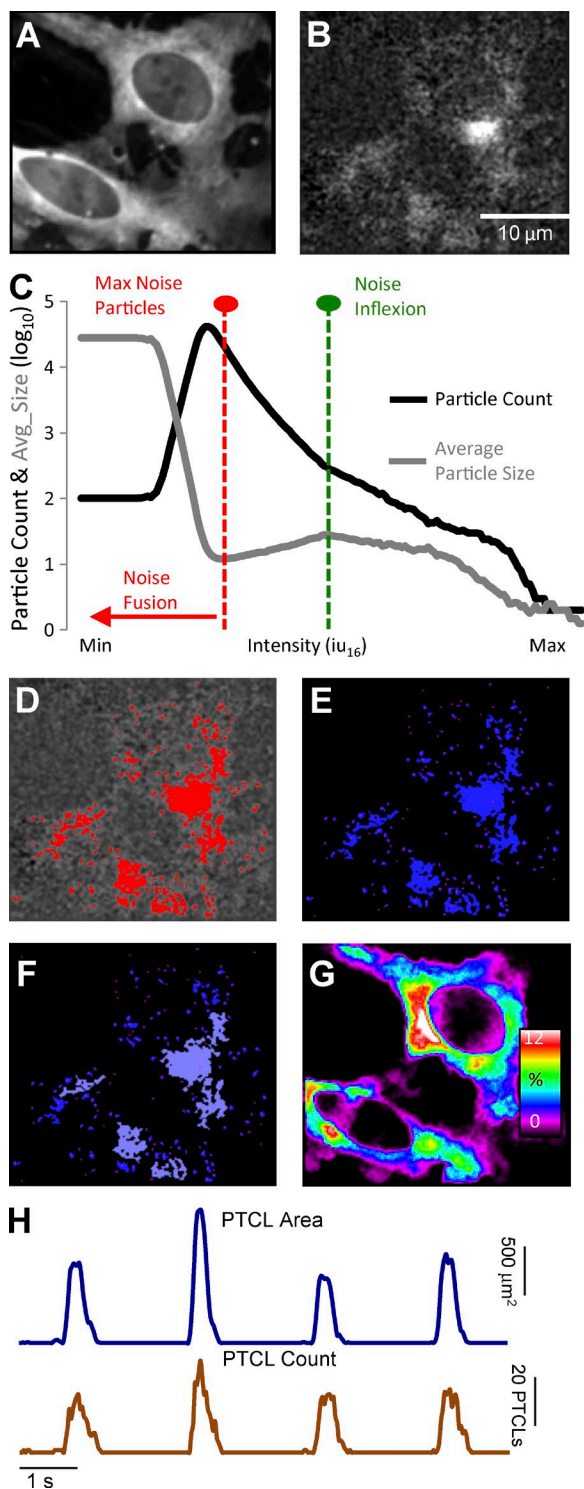
Figure 1. **Analysis of Ca²⁺ transients in ICC-MY.** (A) Representative image of an ICC-MY network from the small intestine of a Kit-Cre-GCaMP3 mouse imaged at 60× magnification. (B) Image taken from the video shown in A after a differential of $\Delta t = \pm 66\text{–}70$ ms and a Gaussian filter of 1.5×1.5 µm, StdDev 1.0 was applied. Scale bar in B applies to A, B, and D–G. (C) Traces of particle count and mean particle size in a thresholding protocol to eliminate noise in the video shown in A (see Materials and methods section Calcium transient analysis for detailed protocol). (D) Image taken from the video in B after threshold-ing was completed with particles above threshold (thresholding protocol shown in C) shown in red. (E) Representative image from the coordinate-based Ca²⁺ particle file created from the thresholded video in D. (F) Representative image taken from the particle file of E after a criteria of >6 µm² (diameter $\sim$2 µm or smaller) was applied; particles above this limit are flagged as purple particles and considered valid PTCLs. (G) Heat map showing the total PTCLs for an entire recording summated with colors representing percentage of occurrence throughout the video (warm colors indicate increased occurrence at that location). (H) Activity traces for PTCLs for the duration of recording from the entire FOV for the representative example shown in A–G. Traces are shown for PTCL area (dark blue) and PTCL count (brown).

TTA-A2 were purchased from Alomone Labs, nicardipine was purchased from Sigma-Aldrich, thapsigargin, isradipine, and ryanodine were purchased from Tocris Bioscience, and multiple batches of Xestospongin C (XeC) were purchased from Cayman Chemical.

Ca²⁺ imaging

After dissections, the muscles were perfused with warmed KRB solution at 37°C for a 1-h equilibration period. Preparations were then visualized and imaged with a spinning-disk confocal microscope (CSU-X1 spinning disk; Yokogawa Electric Corporation) using magnification from 20× to 60×, as previously described (Baker et al., 2015). In brief, images were captured using a high-speed EMCCD Camera (Andor iXon Ultra; ANDOR Technology). Image sequences were collected at 33–105 fps using MetaMorph software (MetaMorph Inc.). Additional Ca²⁺ imaging data were acquired using an Eclipse E600FN microscope (Nikon) equipped with a 60× 1.0 CFI Fluor lens (Nikon). In this system, GCaMP3 was excited at 488 nm (T.I.L.L. Polychrome IV), as previously described (Baker et al., 2013). After acquisition, video sequences of Ca²⁺ imaging data were imported into custom software (Volumetry G8d, written by G.W. Hennig) for analysis. All experiments were performed in the presence of 100 nM nicardipine to reduce movement artifacts. Smooth muscle cells show high expression of Ca²⁺ channels sensitive to dihydropyridines (*Cacna1c*) but low expression in ICC (Chen et al., 2007). Although ICC were shown to express voltage-dependent Ca²⁺ channels encoded by *Cacna1d* (Chen et al., 2007), the concentration of nicardipine used in this study to stabilize movements should have had minimal effects on *Cacna1d* (Ca$_V$ 1.3 channels; Xu and Lipscombe, 2001). In experiments with pharmacological agents, a control activity period (30 s) was recorded, and then solutions containing the drugs were perfused into the chamber for 12 min to allow full tissue penetration. Then a second 30-s recording was made to ascertain the drug effect on ICC-MY activity.

Simultaneous electrophysiological and Ca²⁺ imaging experiments

Jejunal muscle strips (8 × 15 mm) were pinned with tungsten wire (50-μm diameter) with serosa facing upwards to a thin sheet of Sylgard that had nylon mesh attached across a rectangular hole (5 × 10 mm). The Sylgard was inverted in a 35-mm Corning dish with a 20-mm hole in the bottom covered by a 25-mm glass coverslip. Tissues were held against the coverslip using parallel platinum wires placed on either side of the tissue.

Calcium imaging of ICC-MY networks was performed using a confocal spinning disk (CSU-X1 spinning disk; Yokogawa Electric Corporation) mounted on an IX70 inverted microscope (Olympus) and equipped with an Ixon⁺ Ultra 897 camera (Andor). Images were collected using Solis Software (Oxford Instruments) at 50 Hz using 20, 40, and 60× objectives. Simultaneous intracellular microelectrode recordings were performed as previously described (Ward et al., 1994). In brief, impalements of circular muscle cells were made with glass microelectrodes having resistances of 80–120 MΩ. Transmembrane potentials were recorded with a high impedance electrometer (900A) and Digidata (1440A; Axon Instruments) and recorded on a PC running AxoScope 10 data acquisition software (Axon Instruments). Hard copies were made using Clampfit analysis software (Axon Instruments). Experiments were performed in the presence of 1 μM nicardipine to reduce contractions and facilitate impalements of cells for extended periods. It has been previously demonstrated that slow waves in the murine intestine are not significantly affected by nicardipine; however, action potentials initiated in smooth muscle cells are inhibited by this compound (Ward et al., 1994). Microelectrode impalements were made near the center of the FOV in all experiments (see Fig. 5 C). The AxoScope software was triggered from the Andor Solis software used to record images.

Patch-clamp experiments

HEK293 cells with stable expression of $Ca_V3.2$, T-type Ca^{2+} channel, were donated by E. Perez-Reyes (University of Virginia, Charlottesville, VA). HEK-293 cells were maintained in DMEM/F-12 (Thermo Fisher Scientific/Gibco) with FBS (10% [vol/vol]; Gibco), penicillin-streptomycin (1% [vol/vol]; Gibco), and sodium pyruvate (1% [vol/vol]; Gibco) as described previously (Zhu et al., 2016).

The dialyzed whole cell patch-clamp technique was used to record currents activated by application of voltage steps from −80 to 40 mV in 10-mV increments from a holding potential of −80 mV. Cs⁺-rich internal solution contained (mM) 135 CsCl, 3 MgATP, 0.1 NaGTP, 10 BAPTA, 10 HEPES, and 10 glucose adjusted to pH 7.2 with Tris. External solution was a Ca^{2+}-containing physiological salt solution (CaPSS) consisting of (mM)

5 KCl, 135 NaCl, 2 CaCl₂, 10 glucose, 1.2 MgCl₂, and 10 Hepes adjusted to pH 7.4 with Tris. Pipettes with a resistance of 1∼3 MΩ were used for patch-clamp recordings.

Cell sorting and quantitative PCR (qPCR) experiments

Kit$^{+/copGFP}$ mice (B6.129S7-$^{Kittm1Rosay/J}$; 5–8 wk old), bred in house, were used for studies of gene expression in ICC (Ro et al., 2010). These mice allow unequivocal identification of ICC caused by the expression of cop-GFP. After dispersing cells, ICC were purified by fluorescence-activated cell sorting (FACS; Baker et al., 2016), and total RNA was isolated using an Illustra RNAspin Mini RNA Isolation kit (GE Healthcare). qScript cDNA SuperMix (Quanta Biosciences) was used to synthesize first-strand cDNA by the manufacturer's instructions. qPCR was performed with gene-specific primers (Table S2) using Fast Sybr green chemistry on the 7900HT Fast Real-Time PCR System (Applied Biosystems). Regression analysis was used to produce standard curves from the mean values of technical triplicate qPCRs of log10 diluted cDNA samples. Unknown amounts of mRNA were plotted relative to the standard curve for each set of primers using Microsoft Excel. This gave transcriptional quantification of each gene relative to the endogenous *Gapdh* standard after log transformation of the corresponding raw data. Evaluation of gene expression in ICC was compared with expression in the unsorted cell population cells from small intestinal muscles of Kit$^{+/copGFP}$ mice.

Calcium transient analysis

Video preparation. In a previous study, we recorded Ca^{2+} transients from ICC-DMP in the mouse small intestine using KitGCaMP3 mice (Baker et al., 2016). In the current study, we focused exclusively on imaging ICC-MY. Differentiation between ICC-MY and ICC-DMP was based on the following. (a) Their stereotypical anatomical localizations with muscles: ICC-DMP are located within a few cells from the submucosal edge of the circular muscle layer, and ICC-MY are located between the longitudinal and circular muscle layers (Komuro, 2006). (b) Exclusive imaging of one population or the other was facilitated by confocal microscopy and by the orientation of muscle being imaged. (c) The morphology of the two types of ICC is distinct: ICC-MY are stellate and form an interconnected network and ICC-DMP are spindle shaped and not connected in a network (Komuro, 2006).

Videos of Ca^{2+} transients in ICC-MY were imported into Volumetry G8d and motion stabilized (Fig. 1 A). Videos were differentiated (Δt = ±66–70 ms), background subtracted, and smoothed (Gaussian filter: 1.5 × 1.5 μm, StdDev 1.0; Fig. 1 B). To consistently identify Ca^{2+} transients in relation to background intensity levels, a particle analysis routine was run on every video that progressively stepped the intensity threshold from
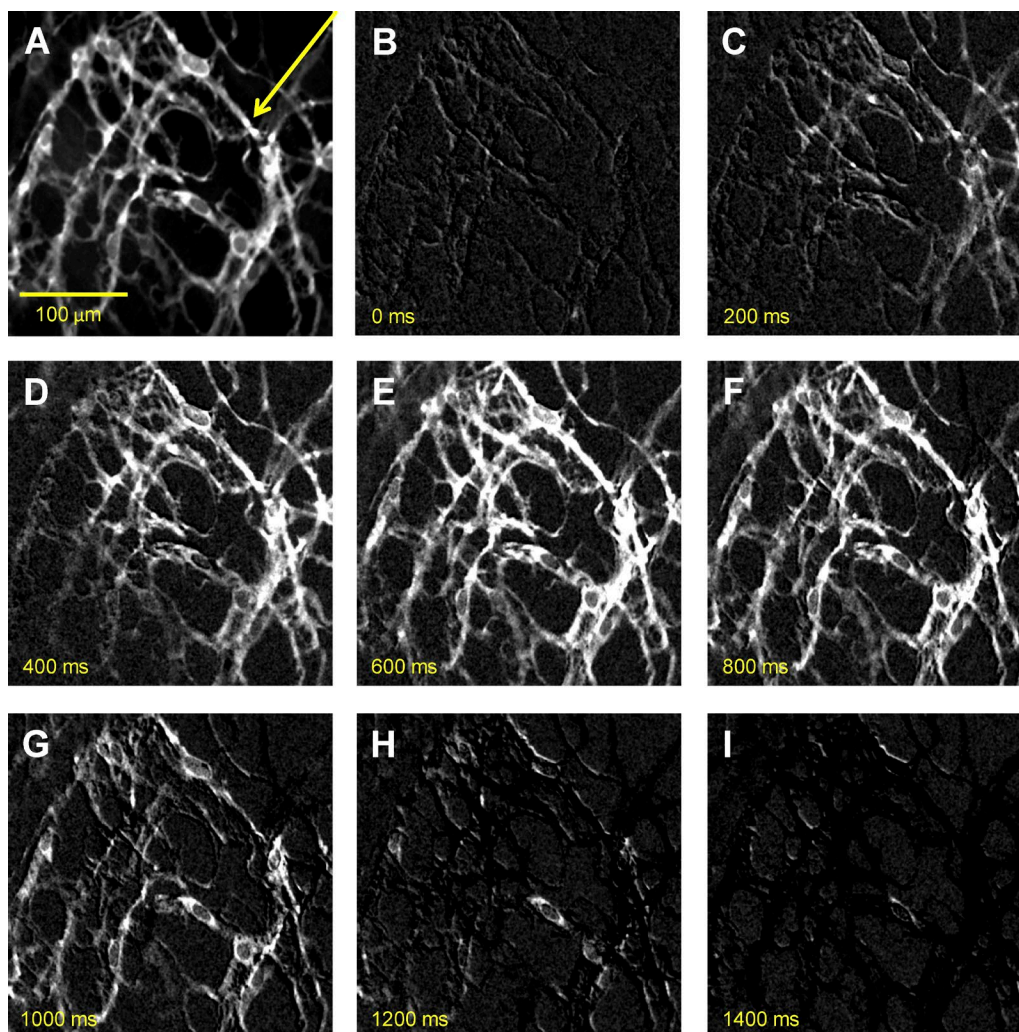
Figure 2. **Propagating Ca²⁺ waves in ICC-MY network.** (A) An image of ICC-MY network from the small intestine of a Kit-Cre-GCaMP3 mouse visualized at 20× magnification. (B–I) Representative montage of the propagation of a Ca²⁺ wave throughout the ICC-MY network. All images in B–I were differentiated ($\Delta t = \pm 66$–70 ms; see Materials and methods) to minimize background noise. The scale bar in A pertains to all other panels. The yellow arrow in A indicates the direction of Ca²⁺ transient propagation.

maximum to minimum. Particles were created using a flood-fill algorithm that marked the structure of all adjoining pixels that had intensities above the threshold (see Winbush et al., 2015). Ca²⁺ transient particles (PTCLs) were larger than background noise particles. The threshold at which noise particles emerged and began to reduce the mean size of particles was used as a common reference threshold for all videos (Fig. 1, C and D). PTCLs representing the areas in cells experiencing Ca²⁺ transients were saved as a coordinate-based particle video (Fig. 1 E).

PTCL analysis. Particles <6 µm² (diameter ~2 µm or smaller) were rejected (Fig. 1 F), and combined area and total number of PTCLs could then be calculated for the entire video (see time courses in Fig. 1 H). Flags (8-bit, bit-hashed, allowing for any combination of seven levels) allowed entire PTCLs to be distinguished

based on whether they met certain spatiotemporal (ST) conditions such as size, shape, compartment overlap (see section on Compartments below) and temporal characteristics. To show the overall regions in cells where Ca²⁺ transients occurred, PTCLs were summed throughout the video to create an image of their occurrence (Fig. 1 G). Analysis could be performed on particles that had one or a combination of flags (e.g., Ca²⁺ transient firing sites in the cell soma).

Compartments. To determine the characteristics of Ca²⁺ transients in cell somata and processes, compartment masks were made from original videos. An overall ICC-MY network structure mask, containing all cellular compartments, was created by averaging all frames in the video (full network mask). Cell somata were selected (cell somata mask). The cell somata mask was subtracted from the full network mask to create a cell
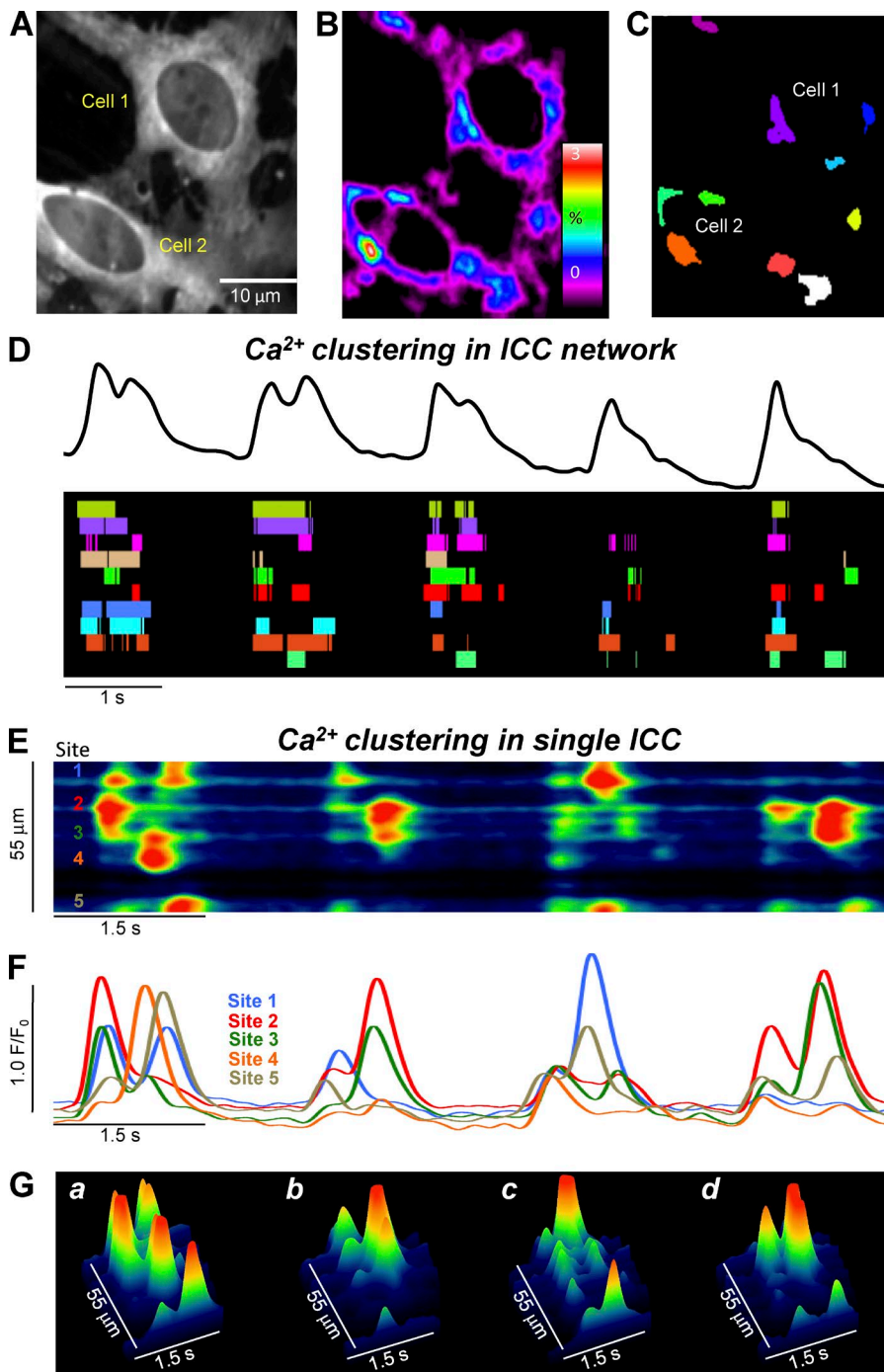
Figure 3. **Ca²⁺ transients in ICC-MY arise from multiple firing sites.** (A) Representative image of an ICC-MY network from the small intestine of a Kit-Cre-GCaMP3 mouse imaged at 60× magnification. (B) Heat map of PTCLs generated from the video shown in A (see method section in Fig. 1). Particles were summated in the resulting heat map to indicate Ca²⁺ firing sites in ICC-MY. (C) Map showing the Ca²⁺ firing sites in the FOV identified in B individually color coded. (D) Ca²⁺ activity trace shown in black (total Ca²⁺ signal of the entire ICC-MY network in FOV) from the video in A over the course of five consecutive CTC cycles. An occurrence map of the activity of individual firing sites is shown below the trace. The temporal characteristics of each individually color coded firing site are displayed as a striped occurrence map, with each "lane" representing the occurrence of PTCLs within each single firing site. (E) ST map of CTCs from the soma of cell 1 (single ICC) from the video in A showing four consecutive CTC cycles. Ca²⁺ activity is color coded with warm areas (red, orange) representing bright areas of Ca²⁺ fluorescence and cold colors (blue, black) representing dim areas of Ca²⁺ fluorescence. Five distinct firing sites within CTCs are marked on the left of the ST map. (F) Traces of the CTCs at each of the five distinct Ca²⁺ firing sites shown on the ST map in E. (G) 3-D surface plots showing the Ca²⁺ activity at the five distinct Ca²⁺ firing sites shown on the ST map in E over four consecutive CTC cycles.

processes mask. Compartment masks were then applied to the particle video of Ca²⁺ transients, and those that overlapped with a particular compartment mask were flagged.

PTCL temporal clustering. The occurrence of Ca²⁺ transients in ICC-MY was temporally clustered with one or more Ca²⁺ transients occurring over time, followed by a period of quiescence. To more consistently identify temporal clusters, the period of time in which PTCLs were separated by <300 ms was marked as a Ca²⁺ tran-

sient cluster (CTC). CTCs allowed the temporal sequence of PTCLs to be quantified on a cycle-to-cycle basis and allowed more precise identification of firing sites. To better isolate firing sites, only those particles that did not overlap with any particles in the previous frame but overlap with particles in the next 70 ms were considered firing sites.

Additional analysis by the creation of ST maps to display Ca²⁺ transient activity was performed using ImageJ software (National Institutes of Health) as described previously (Drumm et al., 2015; Baker et al., 2016).
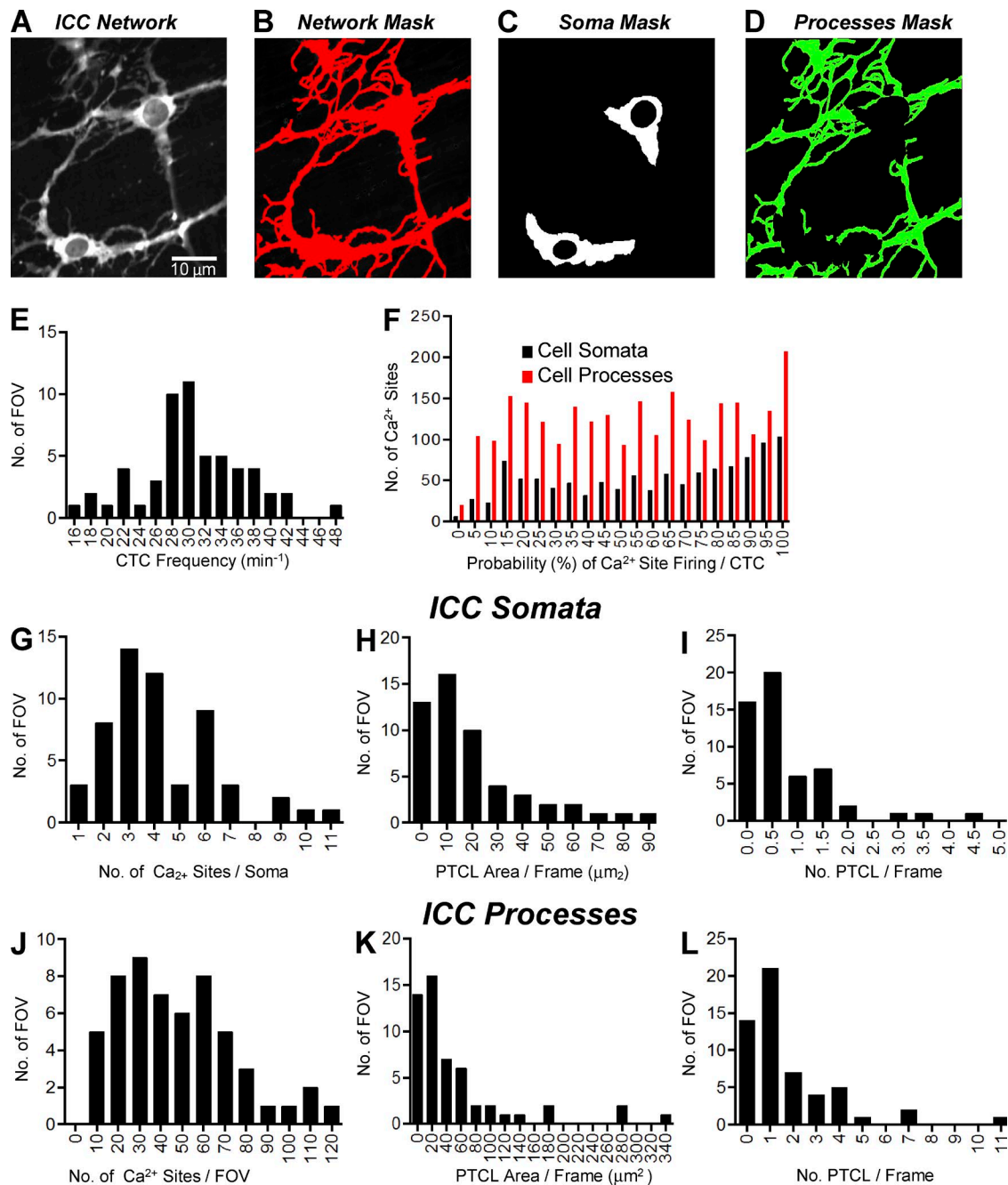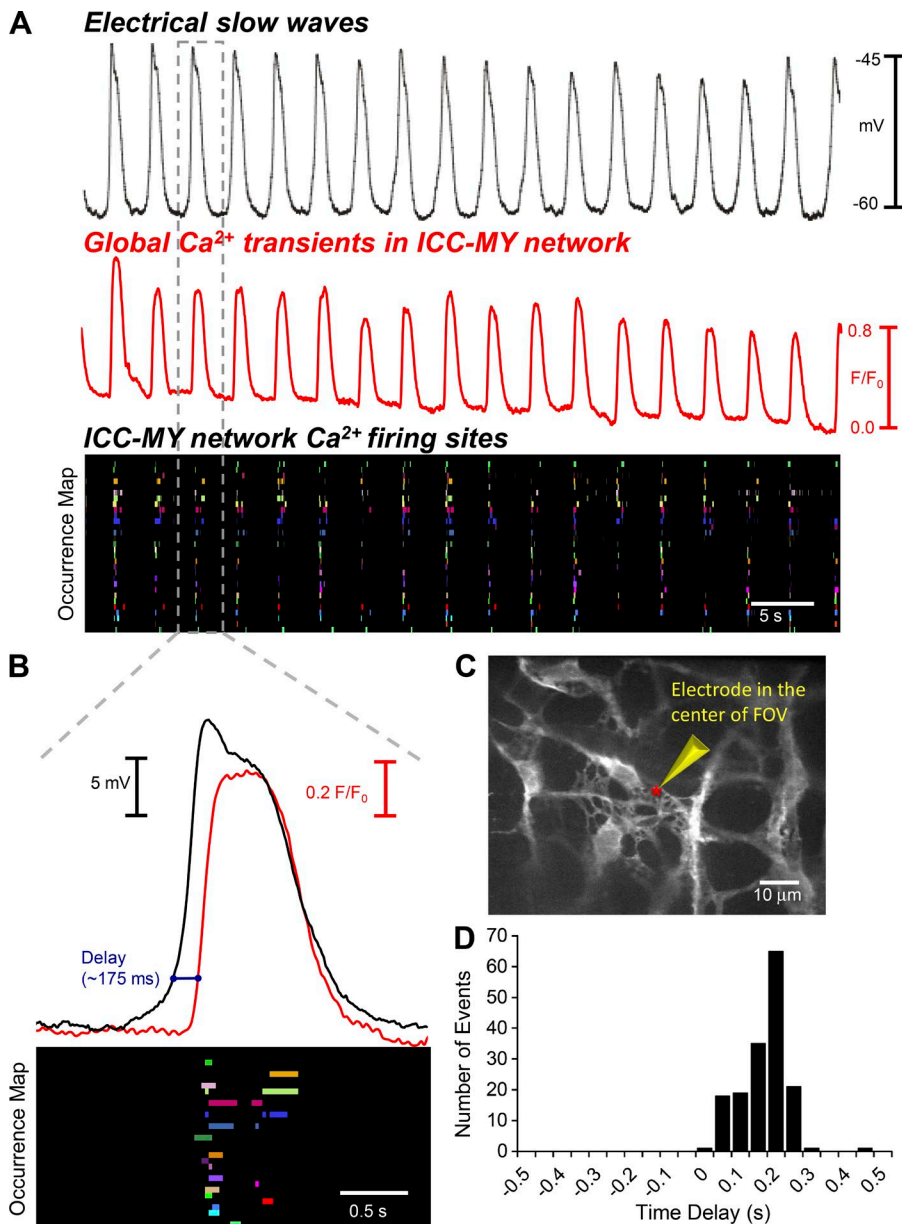
Figure 4. **Quantification of Ca²⁺ transients in ICC-MY.** (A) Representative image of an ICC-MY network from the small intestine. Scale bar in A applies to A–D. (B) Full network mask of the ICC-MY network taken from the video shown in A. (C) Cell somata mask of the ICC-MY taken from the video shown in A. (D) Cell processes mask of the cellular processes of the ICC-MY network taken from the video shown in A. (E) Histogram showing the frequencies of CTCs in the ICC-MY network ($n = 31$, FOV = 56). (F) Histogram showing the probability (%) that an individual Ca²⁺ firing site in the ICC-MY cell somata (black bars) and cell processes (red bars) will fire during a CTC cycle ($n = 31$, FOV = 56). (G) Histogram showing the range of number of Ca²⁺ firing sites per cell soma in ICC-MY ($n = 31$, FOV = 56). (H) Histogram showing the range of values for Ca²⁺ transient PTCL area/frame in the ICC-MY cell somata ($n = 31$, FOV = 56). (I) Histogram showing the range of values for Ca²⁺ transient PTCL count/frame in the ICC-MY cell somata ($n = 31$, FOV = 56). (J) Histogram showing the range of number of Ca²⁺ firing sites per cell processes FOV (60× magnification) in ICC-MY ($n = 31$, FOV = 56). (K) Histogram showing the range of values for Ca²⁺ transient PTCL area/frame in the ICC-MY cell processes ($n = 31$, FOV = 56). (L) Histogram showing the range of values for Ca²⁺ transient PTCL count/frame in the ICC-MY cell processes ($n = 31$, FOV = 56).

Statistical analysis

Data are presented as the mean ± SE unless otherwise stated. Statistical analysis was performed using either a Student's t test or a Mann-Whitney nonparametric test where appropriate. In the case of multiple nonparametric comparisons, a Kruskal-Wallis analysis followed by a

A *Electrical slow waves*

-45
mV
-60

Global Ca²⁺ transients in ICC-MY network

0.8
F/F₀
0.0

ICC-MY network Ca²⁺ firing sites

Occurrence Map

5 s

B

5 mV
0.2 F/F₀

Delay
(~175 ms)

Occurrence Map

0.5 s

C

Electrode in the center of FOV

10 µm

D

Number of Events
70
60
50
40
30
20
10
0

-0.5 -0.4 -0.3 -0.2 -0.1 0 0.1 0.2 0.3 0.4 0.5
Time Delay (s)

Figure 5. **Simultaneous recordings of Ca²⁺ firing in ICC-MY and electrical slow waves.** (A) Representative recording of electrical slow waves (black trace) recorded from the circular smooth muscle layer of murine small intestine from a Kit-Cre-GCaMP3 mouse and simultaneously recorded Ca²⁺ transients (red trace) obtained from the total ICC-MY Ca²⁺ signal from the entire FOV of recording at 60× magnification. An occurrence map showing the pattern of firing of color coded individual Ca²⁺ firing sites from the ICC-MY network in the entire FOV is shown in the below trace. (B) Expanded example of a single electrical slow wave (black) and entire ICC-MY FOV Ca²⁺ transients (red) and Ca²⁺ firing site occurrence map (event 3 from A, as indicated by the projections of the doted gray box). Note the delay between electrical and Ca²⁺waves is ~175 ms (blue line). (C) Representative image of ICC-MY network recorded during intracellular electrical recording; the red asterisks indicate the position of the recording electrode. (D) Frequency histogram of time delays between electrically recorded slow waves in the circular smooth muscle layer and subsequent Ca²⁺ responses of ICC-MY in the field of view ($n = 8$).

Dunn's post-hoc test was performed. In all tests, $P < 0.05$ was considered significant. When describing data, *n* refers to the number of animals used in a dataset whereas FOV refers to the numbers of fields of view used in that same dataset. Note that in figures containing frequency histograms, values were allocated into bins, and the x-axis on these graphs indicates the bin center.
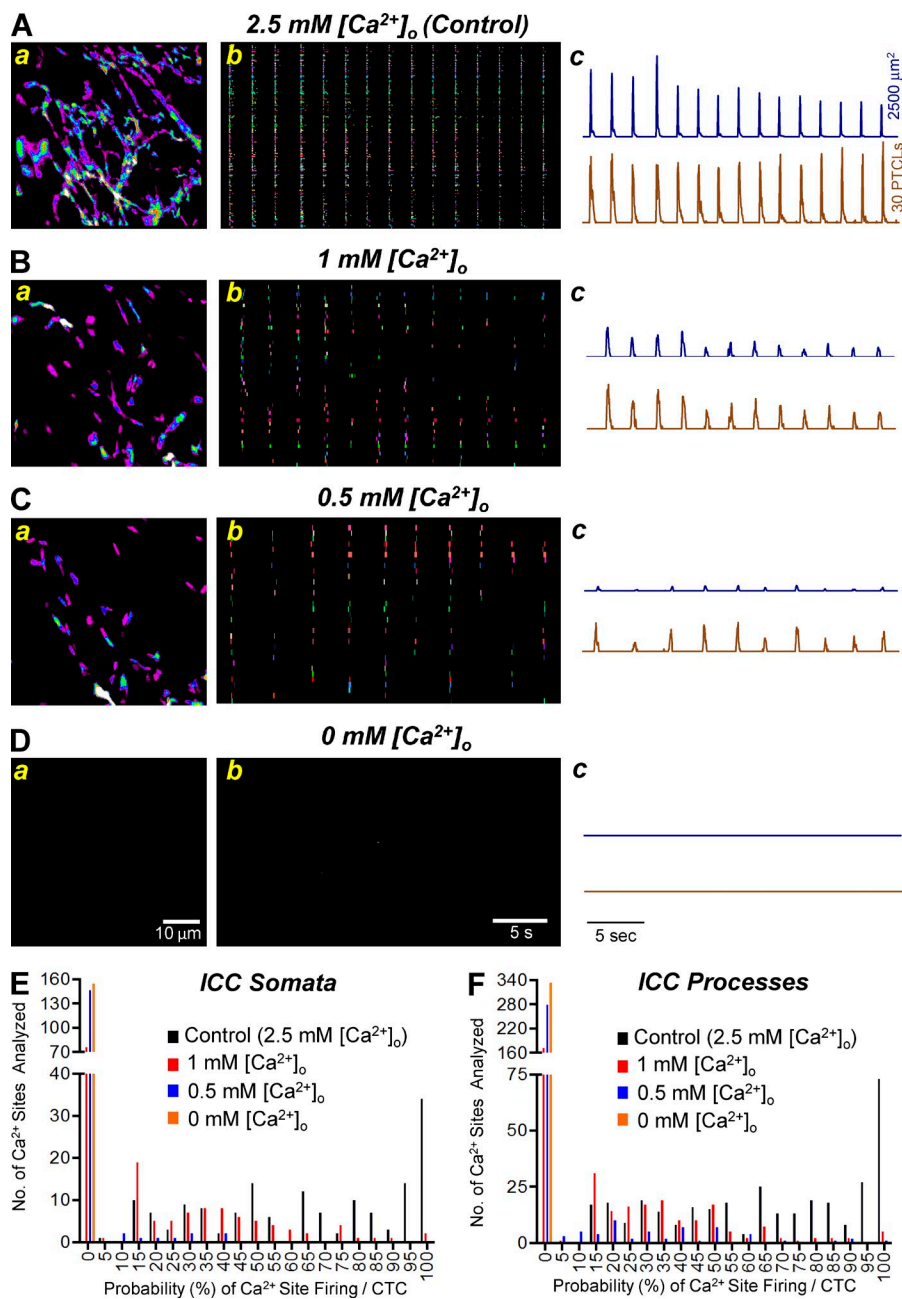
Online supplemental material
Fig. S1 shows molecular expression of Ca²⁺ channel (L and T type) transcripts in ICC. Fig. S2 shows the effect of nicardipine on Ca²⁺ transients in ICC-MY. Fig. S3 shows the effect of isradipine on Ca²⁺ transients in ICC-MY. Fig. S4 shows the effect of the T-type Ca²⁺ channel blockers on electrical slow wave activity. Fig. S5 shows the effects of T-type Ca²⁺ channel blockers on Ca$_V$3.2 currents.

Table S1 quantifies the effects of nicardipine on CTCs in ICC-MY. Table S2 summarizes the gene primers for L- and T-type voltage gated Ca²⁺ channels. Video 1 shows Ca²⁺ waves propagating through an ICC-MY network in murine small intestine. Video 2 shows spontaneous Ca²⁺ transients in ICC-MY.

RESULTS

Spontaneous Ca²⁺ transients in ICC-MY networks were monitored initially at low magnification (20×) to visualize Ca²⁺ waves propagating through ICC-MY networks in small intestinal muscles from Kit-Cre-GCaMP3 mice (Fig. 2 and Video 1). Ca²⁺ waves occurred at a frequency of 29.2 ± 2.7 cpm ($n = 3$) in ICC-MY networks and showed a propagation velocity of 1.86 ± 0.25 mm/s,

A **2.5 mM [Ca²⁺]₀ (Control)**

B **1 mM [Ca²⁺]₀**

C **0.5 mM [Ca²⁺]₀**

D **0 mM [Ca²⁺]₀**

E *ICC Somata*
- Control (2.5 mM [Ca²⁺]₀)
- 1 mM [Ca²⁺]₀
- 0.5 mM [Ca²⁺]₀
- 0 mM [Ca²⁺]₀

No. of Ca²⁺ Sites Analyzed — Probability (%) of Ca²⁺ Site Firing / CTC

F *ICC Processes*
- Control (2.5 mM [Ca²⁺]₀)
- 1 mM [Ca²⁺]₀
- 0.5 mM [Ca²⁺]₀
- 0 mM [Ca²⁺]₀

No. of Ca²⁺ Sites Analyzed — Probability (%) of Ca²⁺ Site Firing / CTC

Figure 6. **The effect of lowering [Ca²⁺]₀ on Ca²⁺ transients in ICC-MY.** (A) Aa–Ac show normal [Ca²⁺]₀ concentrations (2.5 mM) on ICC-MY Ca²⁺ transients. (Aa) Representative heat map showing the summated PTCLs for an entire recording of ICC-MY in control. (Ab) Occurrence map of individually color-coded Ca²⁺ firing sites in the ICC-MY network under control conditions. (Ac) Traces of PTCL activity over an entire recording of the ICC-MY network under control conditions showing PTCL area (dark blue) and PTCL count (brown). (B) Ba–Bc show the effects of lowering [Ca²⁺]₀ concentrations to 1 mM on ICC-MY Ca²⁺ transients. (Ba) Representative heat map showing the summated PTCLs of ICC-MY in 1 mM [Ca²⁺]₀ conditions. (Bb) Occurrence map of individually color coded Ca²⁺ firing sites in the ICC-MY network in 1 mM [Ca²⁺]₀ conditions. (Bc) Traces of PTCL activity over an entire recording of the ICC-MY network under 1 mM [Ca²⁺]₀ conditions showing PTCL area (dark blue) and PTCL count (brown). (C) Ca–Cc show the effects of lowering [Ca²⁺]₀ concentrations to 0.5 mM on ICC-MY Ca²⁺ transients. (Ca) Representative heat map showing the summated PTCLs of ICC-MY in 0.5 mM [Ca²⁺]₀ conditions. (Cb) Occurrence map of individually color coded Ca²⁺ firing sites in the ICC-MY network in 0.5 mM [Ca²⁺]₀ conditions. (Cc) Traces of PTCL activity of the ICC-MY network in 0.5 mM [Ca²⁺]₀ conditions showing PTCL area (dark blue) and PTCL count (brown). (D) Da–Dc shows the effects of removing [Ca²⁺]₀ from the external solution on ICC-MY Ca²⁺ transients. (Da–Dc) Representative heat map showing the summated PTCLs for ICC-MY in 0 mM [Ca²⁺]₀ conditions shows no Ca²⁺ activity as shown in the occurrence map (Db) and traces of Ca²⁺ transients (Dc). (E) Summary histogram showing the probability (%) that an individual Ca²⁺ firing site in the ICC-MY cell soma will fire during a CTC cycle in control conditions (black bars), 1 mM [Ca²⁺]₀ (red bars), 0.5 mM [Ca²⁺]₀ (blue bars) and 0 mM [Ca²⁺]₀ (orange bars; *n* = 5, FOV = 6). (F) Summary histogram showing the probability of an individual Ca²⁺ firing site in the ICC-MY cell processes will fire during a CTC cycle (*n* = 5, FOV = 6).

which is similar to Ca²⁺ waves visualized previously in ICC-MY networks loaded with Fluo4-AM (Park et al., 2006). However, rather than detecting a global rise and fall in fluorescence as previously observed, ICC-MY of Kit-Cre-GCaMP3 mice displayed asynchronous subcellular bright spots that flickered on and off for several

hundred milliseconds during each cycle. These subcellular Ca²⁺ transients were explored in more detail.

Ca²⁺ transients arise from multiple sites within ICC-MY
Higher power imaging (60× objective) resolved localized subcellular Ca²⁺ transients (Fig. 3 A and Video 2).

Table 1. **Quantifying the effect of lowering $[Ca^{2+}]_o$ on CTCs in ICC-MY**

CTC parameters	2.5 mM $[Ca^{2+}]_o$	1 mM $[Ca^{2+}]_o$	0.5 mM $[Ca^{2+}]_o$	0 mM $[Ca^{2+}]_o$
Probability (%) of Ca^{2+} site firing/CTC cycle (somata)	64.7 ± 2.3	19.8 ± 1.9	1.4 ± 0.5	0
Probability (%) of Ca^{2+} site firing/CTC cycle (processes)	65.7 ± 1.6	18.2 ± 1.3	5.8 ± 0.9	0
No. of Ca^{2+} sites/soma	4.8 ± 1	2.09 ± 0.27	0.29 ± 0.07	0
No. of Ca^{2+} sites/process FOV	55.67 ± 13	27.67 ± 3.96	9.33 ± 4.04	0
PTCL area/frame (μm^2) somata	30.77 ± 10.23	6.73 ± 1.76	0.28 ± 0.18	0
PTCL area/frame (μm^2) processes	80.71 ± 29	13.17 ± 2.88	15.67 ± 13.23	0
PTCL count/frame somata	0.84 ± 0.2	0.28 ± 0.06	0.02 ± 0.01	0
PTCL count/frame processes	2.28 ± 0.56	0.71 ± 0.14	0.13 ± 0.08	0

The localized events were analyzed within networks and in individual cells using PTCL analysis, as described in Materials and methods (see Fig. 1). We identified all firing sites in cells within a FOV (Fig. 3 B), which were color coded separately (Fig. 3 C and Video 2). In the example shown in Fig. 3 C, each cell contained five distinct Ca^{2+} firing sites. Summation of the Ca^{2+} transients in the FOV represented the periodic rise and fall of Ca^{2+} in the ICC-MY network (global Ca^{2+} oscillations) as shown in the top panel of Fig. 3 D. However, when the activity of each Ca^{2+} firing site in Fig. 3 C was plotted as an occurrence map (Fig. 3 D, bottom), with each colored "lane" representing a single firing site, it became clear that the network Ca^{2+} oscillations resulted from summation of many, distinct firing sites that occurred asynchronously within the timeframe of each global Ca^{2+} cycle. The activities of the firing sites were organized into temporal clusters (columns of firing events in the occurrence map). Closer inspection of the occurrence map (Fig. 3 D) revealed that not every site fired during each cycle, the sequence of firing changed from cycle to cycle, and during some temporal clusters, sites fired more than once. The temporal Ca^{2+} clusters are henceforth referred to as CTCs. Detailed analysis of CTCs within single ICC in a network (Fig. 3, E–G) also showed asynchronous clustering of events from multiple Ca^{2+} firing sites.

Quantification of Ca^{2+} transients in ICC-MY
Ca^{2+} transients in ICC-MY (cell somata and cell processes) were quantified in whole networks of ICC (Fig. 4, E–L). Ca^{2+} transients within specific regions of the ICC-MY were tabulated using cell somata and process masks (Fig. 4, C and D) as described in the Materials and methods.

The frequency of CTCs within ICC networks varied from 16 to 48 cycles per min, with a mean of 30.4 ± 0.8 cpm (Fig. 4 E, $n = 31$, FOV = 56). The frequencies of CTCs corresponded well with the frequencies of electrical slow waves recorded from murine small intestine (Ward et al., 1994; Ördög et al., 1999; Kito et al., 2005; Sanders et al., 2014).

The dynamics of the Ca^{2+} transients within CTCs was variable (Fig. 4, F–L). The probability that individual Ca^{2+} firing sites activated during a CTC varied in both cell somata and processes (Fig. 4 F). Across the experiments performed, the probability of firing for Ca^{2+} sites per CTC in cell somata was $59.6 \pm 0.9\%$ ($n = 31$, FOV = 56). Firing sites in the cell processes displayed a similar mean probability of firing during a CTC of $54.2 \pm 0.6\%$ ($n = 31$, FOV = 56).

The number of firing sites averaged 4.2 ± 0.3 per cell soma (Fig. 4 G, $n = 31$, FOV = 56). The number of Ca^{2+} firing sites in processes of ICC-MY averaged 46.7 ± 3.6 per FOV (60× objective, Fig. 4 J, $n = 31$, FOV = 56). Standardization of PTCL area and count were made by summating the total PTCL area or total PTCL count and dividing the value by the number of frames in a given recording, giving values of PTCL area/frame and PTCL count/frame. In the experiments performed, PTCL area/frame of cell somata averaged 20.6 ± 3 μm^2 ($n = 31$, FOV = 56; Fig. 4 H) and PTCL count/frame in the somata averaged 0.76 ± 0.1 (Fig. 4 I, $n = 31$, FOV = 56). PTCL area/frame in processes averaged 54.1 ± 10 μm^2 (Fig. 4 K, $n = 31$, FOV = 56) and PTCL count in the processes averaged 1.8 ± 0.3 (Fig. 4 L, $n = 31$, FOV = 56).

Ca^{2+} oscillations (CTCs) in ICC-MY are associated with electrical slow waves
Ca^{2+} waves propagating through ICC-MY networks are associated with electrical slow waves in the small intestine (Park et al., 2006; Lee et al., 2007). We sought to confirm this relationship in muscles from Kit-Cre-GCaMP3 mice, to define the temporal relationship between slow waves and CTCs, and to determine whether the duration of CTCs corresponds to the slow wave duration.

Intracellular electrical recordings were made from jejunal muscles of Kit-Cre-GCaMP3 mice, which displayed slow wave activity, as previously reported (Baker et al., 2016). Simultaneous Ca^{2+} imaging of ICC-MY networks near impaled cells showed that Ca^{2+} waves propagating across ICC-MY networks occurred on a 1:1 basis with slow waves (Fig. 5 A).

Occurrence maps of Ca^{2+} firing sites in Fig. 5 A show that the Ca^{2+} transients were organized into CTCs and approximately in phase with slow waves. Closer inspection and superposition of summed network Ca^{2+} transients, occurrence maps, and slow waves showed that there was a delay in which the upstroke depolarization of the slow waves slightly preceded the onset of the CTCs
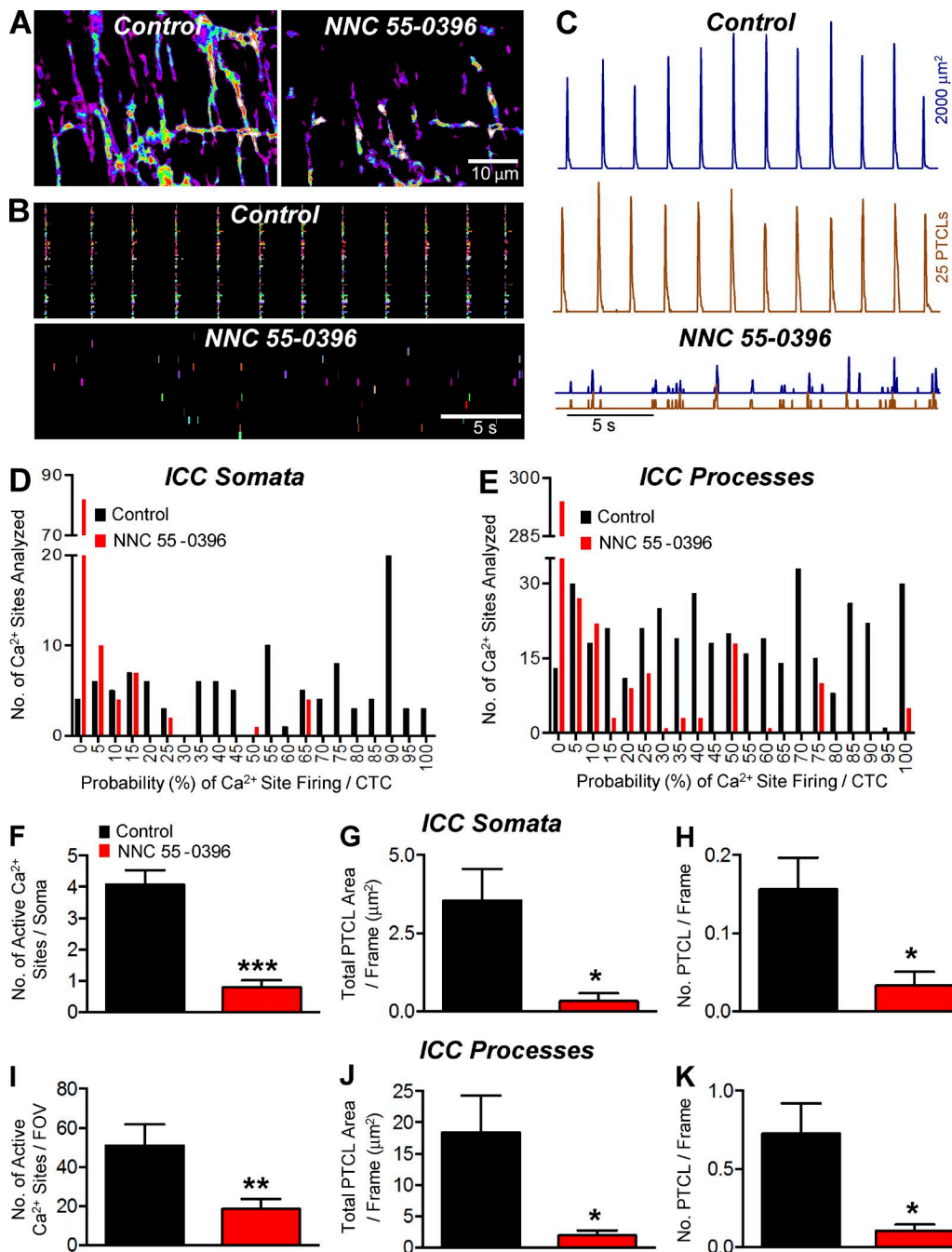
Figure 7. **The effect of NNC 55-0396 on Ca²⁺ transients in ICC-MY.** (A) Representative heat maps showing the summated PTCLs for an entire recording of ICC-MY under control conditions and in NNC 55-0396 (1 µM). (B) Occurrence map of individually color coded Ca²⁺ firing sites in the ICC-MY network in control and NNC 55-0396 (1 µM) conditions. (C) Traces of PTCL activity of the ICC-MY network in control conditions and in the presence of NNC 55-0396 (1 µM) showing PTCL area (dark blue) and PTCL count (brown). (D) Histogram showing the probability (%) that an individual Ca²⁺ firing site in the ICC-MY cell somata will fire during a CTC cycle under control conditions (black bars) and in NNC 55-0396 (1 µM; red bars; $n = 6$, FOV = 8). (E) Histogram showing the probability (%) that an individual Ca²⁺ firing site in the ICC-MY cell processes will fire during a CTC cycle in control conditions (black bars) and in NNC 55-0396 (1 µM; red bars; $n = 6$, FOV = 8). (F) The number of Ca²⁺ firing sites in the cell soma was reduced from 4.1 ± 0.5 sites per cell in control to 0.8 ± 0.2 sites per cell in NNC 55-0396 (1 µM; $P = 0.0009$, $n = 6$, FOV = 8). (G) PTCL area/frame in the cell somata were reduced from 3.5 ± 1 µm² in control to 0.3 ± 0.25 µm² in NNC 55–0396 (1 µM; $P = 0.017$, $n = 6$, FOV = 8). (H) PTCL count/frame was significantly reduced in the cell somata from 0.16 ± 0.04 in control to 0.03 ± 0.02 in NNC 55-0396 (1 µM; $P = 0.022$, $n = 6$, FOV = 8). (I) In the cell processes, the number of Ca²⁺ firing sites was reduced from 51 ± 10.7 per FOV in control to 18.5 ± 5.1 per FOV in NNC 55-0396 (1 µM; $P = 0.005$, $n = 6$, FOV = 8). (J) In the cell processes, PTCL area/frame was reduced from 18.4 ± 5.9 µm² in control to 1.9 ± 0.8 µm² in NNC 55–0396 (1 µM; $P = 0.029$, $n = 6$, FOV = 8). (K) PTCL count/frame was also significantly reduced in the cell processes, changing from 0.7 ± 0.19 in control to 0.1 ± 0.04 in NNC 55-0396 (1 µM; $P = 0.014$, $n = 6$, FOV = 8). *, $P < 0.05$; **, $P < 0.01$; ***, $P < 0.001$. Mean ± SE is shown.
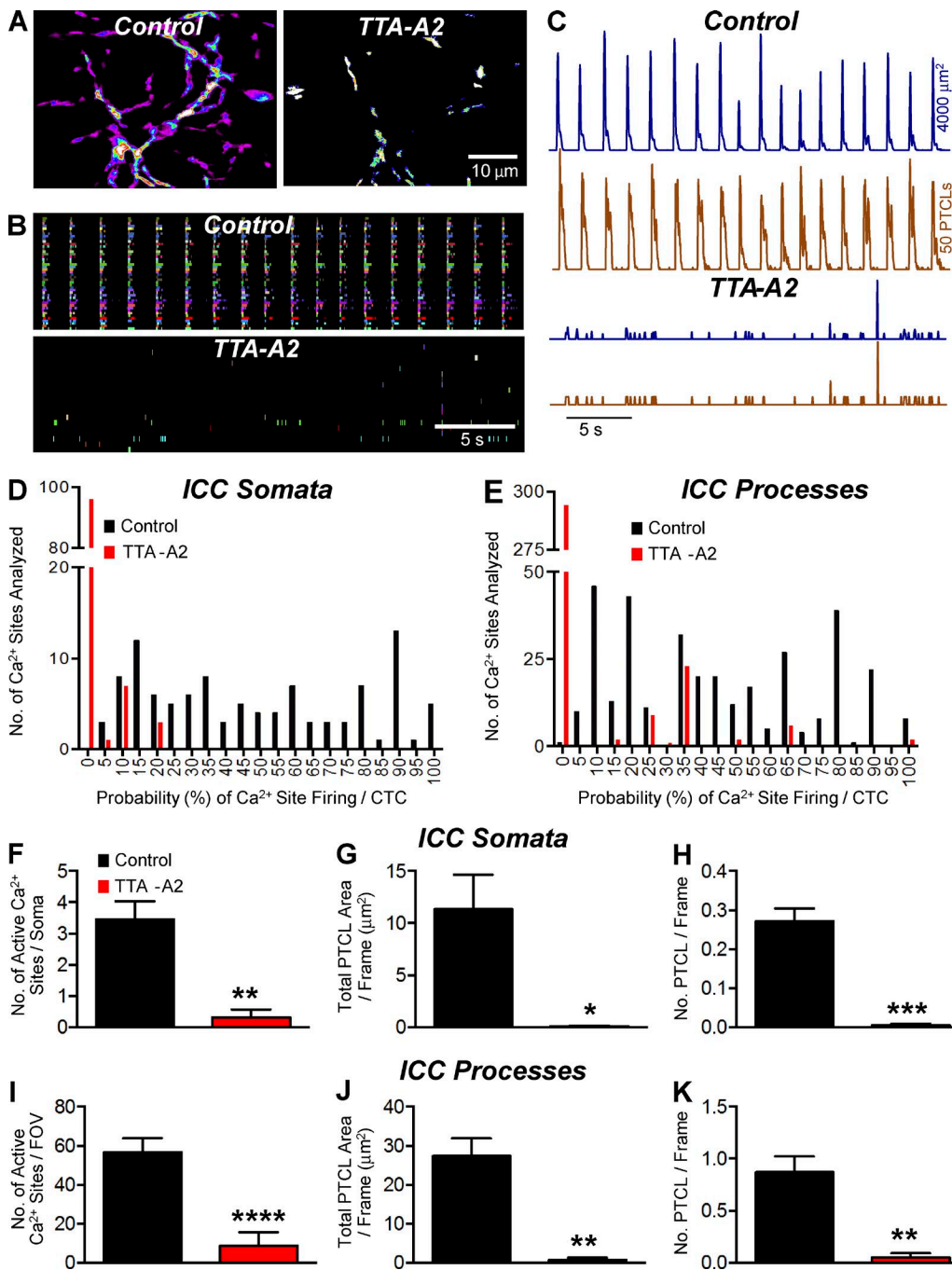
Figure 8.   **The effect of TTA-A2 on Ca²⁺ transients in ICC-MY.** (A) Representative heat map showing the summated PTCLs recording of ICC-MY in control and TTA-A2 (1 µM). (B) Occurrence map of individually color-coded Ca²⁺ firing sites in the ICC-MY network in control and TTA-A2 conditions. (C) Traces of PTCL activity of the ICC-MY network in control conditions and in the presence of TTA-A2 showing PTCL area (dark blue) and PTCL count (brown). (D) Histogram showing the probability (%) that an individual Ca²⁺ firing site in the ICC-MY cell somata will fire during a CTC cycle in control conditions (black bars) and TTA-A2 (1 µM; red bars; n = 5, FOV = 6). (E) Histogram showing the probability (%) that an individual Ca²⁺ firing site in the ICC-MY cell processes will fire during a CTC cycle in control conditions (black bars) and TTA-A2 (1 µM; red bars; n = 5, FOV = 6). (F) The number of firing sites in the cell soma was reduced from 3.5 ± 0.6 in control to 0.3 ± 0.25 in TTA-A2 (1 µM; P = 0.006, n = 5, FOV = 6). (G) In the presence of TTA-A2 (1 µM), the PTCL area/frame in the cell somata was 0.07 ± 0.069 µm² compared with 11.4 ± 3.3 µm² in control (P = 0.0197, n = 5, FOV = 6). (H) The PTCL count/frame in the cell somata was reduced from 0.3 ± 0.03 in control to 0.005 ± 0.0039 in TTA-A2 (1 µM; P = 0.0007 n = 5, FOV = 6). (I) In the cell processes, the number of Ca²⁺ firing sites per FOV was reduced from 56.5 ± 7.4 in control to 8.7 ± 6.9 in TTA-A2 (1 µM; P = 0.0001, n = 5, FOV = 6). (J) The PTCL area/frame in the cell processes was reduced from 27.4 ± 4.8 µm² in control to 0.7 ± 0.59 µm² in the presence of TTA-A2 (1 µM; P = 0.0016 n = 5, FOV = 6). (K) In the cell processes, PTCL count/frame was reduced from 0.87 ± 0.15 in control to 0.05 ± 0.04 in TTA-A2 (1 µM; P = 0.0014 n = 5, FOV = 6). *, P < 0.05; **, P < 0.01; ***, P < 0.001; ****, P < 0.0001. Mean ± SE is shown.
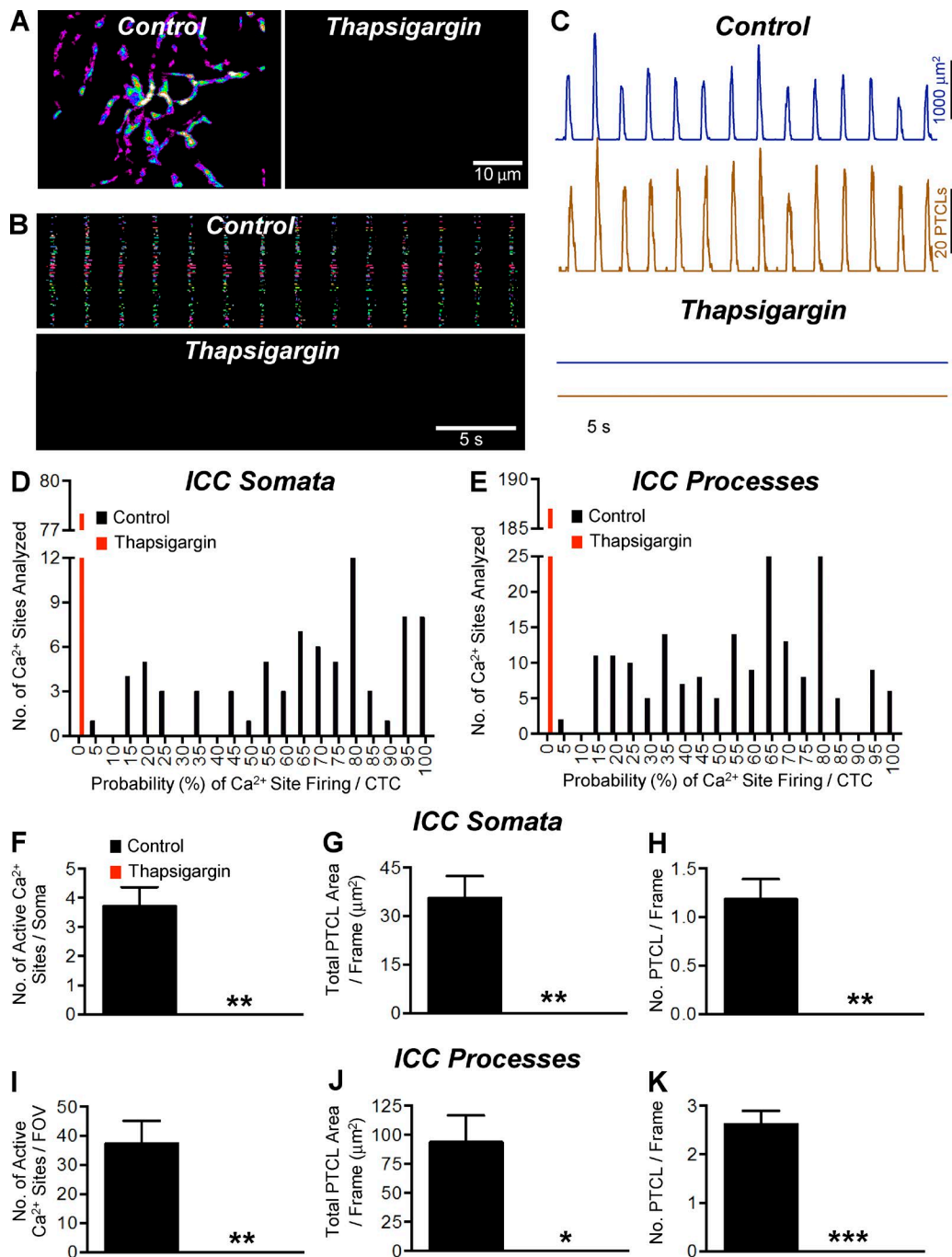
Figure 9. **The effect of thapsigargin on Ca^{2+} transients in ICC-MY.** (A) Representative heat map showing the summated PTCLs for an entire 60× magnification recording of ICC-MY in control and thapsigargin (10 µM). (B) Occurrence map of individually color-coded Ca^{2+} firing sites in the ICC-MY network in control and thapsigargin (10 µM) conditions. (C) Traces of PTCL activity over an entire recording of the ICC-MY network in control conditions and in the presence of thapsigargin (10 µM) showing PTCL area (dark blue) and PTCL count (brown). (D) Histogram showing the probability (%) that an individual Ca^{2+} firing site in the ICC-MY cell somata will fire during a CTC cycle in control conditions (black bars) and thapsigargin (10 µM; red bars; $n = 5$, FOV = 5). (E) Histogram showing the probability (%) that an individual Ca^{2+} firing site in the ICC-MY cell processes will fire during a CTC cycle in control conditions (black bars) and thapsigargin (10 µM; red bars; $n = 5$, FOV = 5). (F) Summary data showing the effect of thapsigargin (10 µM) on the number of active Ca^{2+} firing sites in the cell soma of ICC-MY ($n = 5$, FOV = 5). (G) Summary data showing the effect of thapsigargin (10 µM) on the total PTCL area per frame in the cell somata of ICC-MY ($n = 5$, FOV = 5). (H) Summary data showing the effect of thapsigargin (10 µM) on the total PTCL count per frame in the cell somata of ICC-MY ($n = 5$, FOV = 5). (I–K) Summary data showing the effect of thapsigargin (10 µM) on the number of active Ca^{2+} firing sites (I); total PTCL area per frame (J; $n = 5$, FOV = 5) and total PTCL count per frame (K) in the cell processes ($n = 5$, FOV = 5). *, $P < 0.05$; **, $P < 0.01$; ***, $P < 0.001$. Mean ± SE is shown.
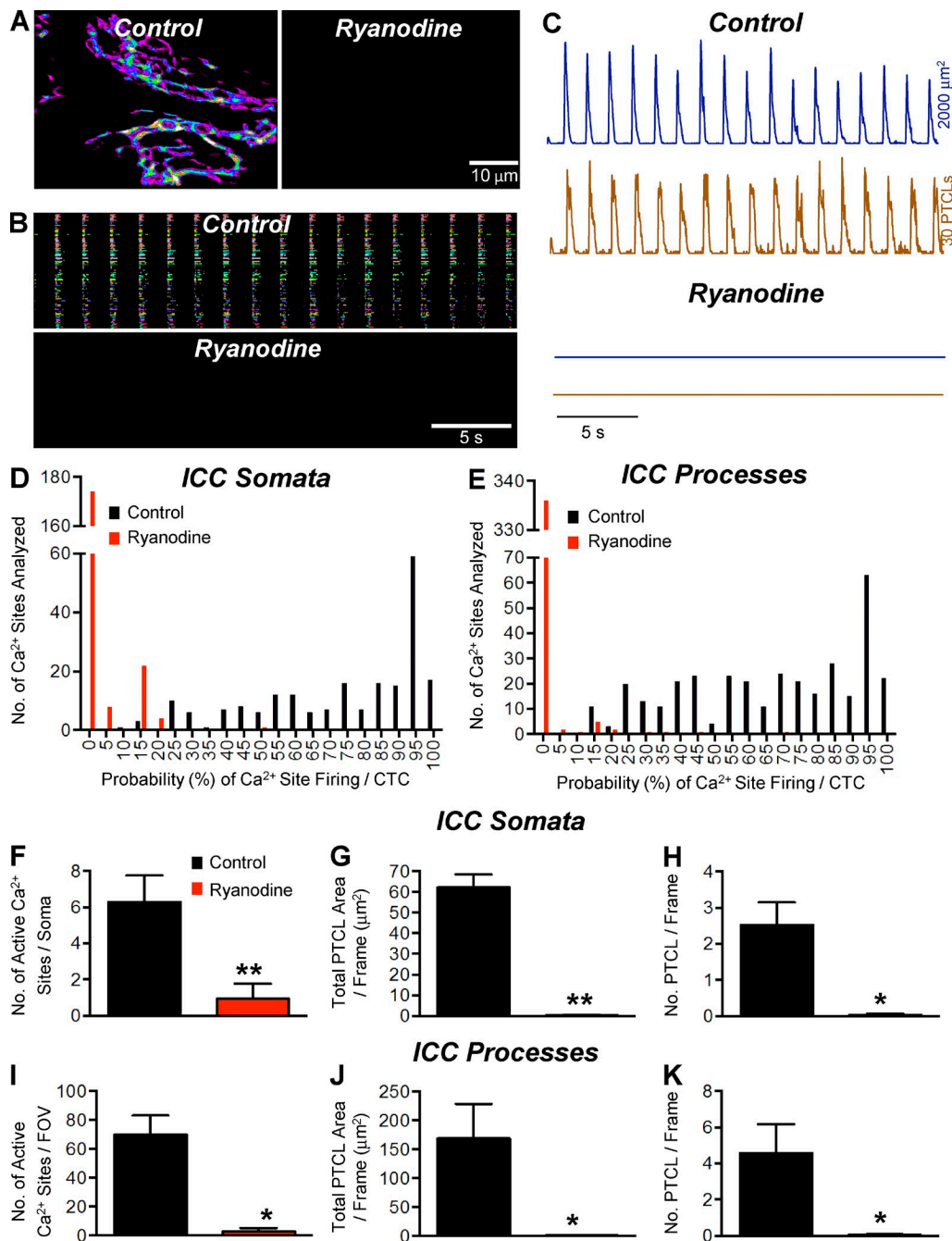
Figure 10. The effect of ryanodine on Ca^{2+} transients in ICC-MY. (A and B) Representative heat map showing the summated PTCLs for an entire 60× magnification recording of ICC-MY in control and ryanodine (100 µM) showing the inhibitory effects of ryanodine (A), as indicated in the occurrence map of individually color-coded Ca^{2+} firing sites in the ICC-MY network (B). (C) Traces of PTCL activity (PTCL area [dark blue] and PTCL count [brown]) in control and ryanodine. (D and E) Histogram showing the probability (%) that an individual Ca^{2+} firing site in the ICC-MY cell somata and cell processes in E will fire during a CTC cycle in control conditions (black bars) and ryanodine (100 µM; red bars; $n = 5$, FOV = 5). (F) The number of Ca^{2+} firing sites per cell soma was reduced from 6.28 ± 1.47 in control to 0.94 ± 0.81 in the presence of ryanodine (100 µM; P = 0.01, $n = 5$, FOV = 5). (G) PTCL area/frame was reduced in the cell somata from 62.19 ± 6.34 µm^2 in control to 0.3 ± 0.2 µm^2 in ryanodine (100 µM; P = 0.002, $n = 5$, FOV = 5). (H) PTCL count/frame was reduced in the cell somata from 2.5 ± 0.63 in control to 0.04 ± 0.03 in ryanodine (100 µM; P = 0.014, $n = 5$, FOV = 5). (I) In the cell processes, the number of Ca^{2+} firing sites per FOV was reduced from 70 ± 13.12 in control to 2.8 ± 2.33 in ryanodine (100 µM; P = 0.011, $n = 5$, FOV = 5). (J) PTCL area/frame was reduced in the cell processes from 169.1 ± 59.46 µm^2 in control to 1.3 ± 1.2 µm^2 in ryanodine (100 µM; P = 0.046, $n = 5$, FOV = 5). (K) PTCL count/frame was reduced in the cell processes from 4.57 ± 1.59 in control to 0.045 ± 0.043 in ryanodine (100 µM; P = 0.014, $n = 5$, FOV = 5). *, P < 0.05; **, P < 0.01. Mean ± SE is shown.
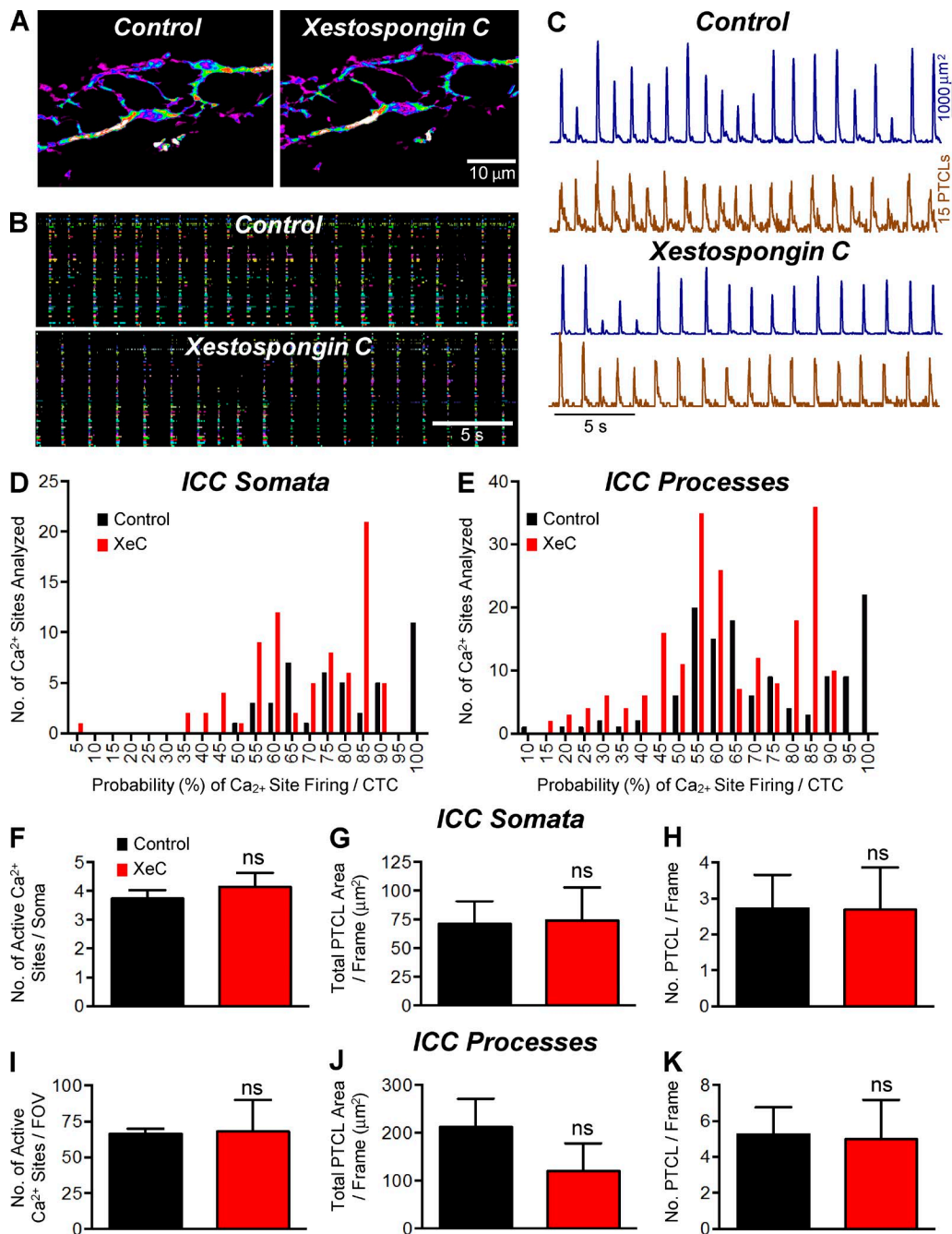
ICC Ca^{2+} transient clustering | Drumm et al.

Figure 11. **The effect of XeC on Ca²⁺ transients in ICC-MY.** (A) Representative heat map showing the summated PTCLs of ICC-MY in control and XeC (10 μM). (B) Occurrence map of individually color-coded Ca²⁺ firing sites in the ICC-MY network in control and XeC conditions. (C) Traces of PTCL activity over an entire recording of the ICC-MY network in control conditions and in the presence of XeC (10 μM) showing PTCL area (dark blue) and PTCL count (brown). (D and E) Histogram showing the probability (%) that an individual Ca²⁺ firing site in the ICC-MY cell somata and cell processes in E will fire during a CTC cycle in the presence of XeC (10 μM; red bars) compared with control conditions (black bars; $n = 3$, FOV = 3). (F) Summary showing that the number of Ca²⁺ firing sites in cell soma was not significantly affected by XeC (10 μM; $P = 0.22$). (G) PTCL area/frame in the cell somata were 71.42 ± 19.54 μm² in control and 74.36 ± 28.58 μm² in XeC (10 μM; $P = 0.86$, $n = 3$, FOV = 3). (H) The PTCL count/frame in the cell soma was 2.71 ± 0.95 in control and 2.69 ± 1.17 in XeC (10 μM; $P = 0.95$, $n = 3$, FOV = 3). (I) The number of Ca²⁺ firing sites in the cell processes per FOV changed from 66.3 ± 3.7 in control to 68 ± 22.05 in XeC (10 μM; $P = 0.93$, $n = 3$, FOV = 3). (J) PTCL area/frame in the cell processes was 212.4 ± 59.47 μm² in control and 120.2 ± 58.21 μm² in XeC (10 μM; $P = 0.12$, $n = 3$, FOV = 3). (K) The PTCL count/frame in the cell processes was 5.27 ± 1.49 in control and 4.98 ± 2.18 in XeC (10 μM; $P = 0.95$, $n = 3$, FOV = 3). ns, $P > 0.05$. Mean ± SE is shown.

in ICC-MY adjacent to the site of impalement (Fig. 5, B and C). Data from these experiments were summarized into a frequency histogram of the delays between electrical slow waves and CTCs in ICC-MY. The mean delay between initiation of the slow wave upstrokes and the first firing of Ca^{2+} transients in CTCs was 175.1 ± 64.2 ms (160 slow waves; $n = 8$). The duration of CTCs (1.15 ± 0.05 s) approximated the duration of slow waves (1.26 ± 0.1 s; $n = 8$).

Involvement of Ca^{2+} influx mechanisms in generating CTCs in ICC-MY

We tested the effects of reducing extracellular Ca^{2+} ($[Ca^{2+}]_o$) on CTCs in ICC-MY. Removal of extracellular Ca^{2+} abolished CTCs within 12 min ($n = 5$). When $[Ca^{2+}]_o$ was decreased in a stepwise manner from 2.5 mM to 0 mM, there was concentration-dependent reduction in Ca^{2+} firing sites as shown in occurrence maps and reductions in PTCL area and PTCL counts (Fig. 6, A–D). Fig. 6 E shows a frequency histogram of Ca^{2+} site firing probability in cell somata when $[Ca^{2+}]_o$ was reduced. Under control conditions (2.5 mM $[Ca^{2+}]_o$), the average probability of an individual Ca^{2+} site firing during a CTC was $64.7 \pm 2.3\%$. When $[Ca^{2+}]_o$ was reduced to 1 mM $[Ca^{2+}]_o$, the probability decreased to $19.8 \pm 1.9\%$ and to $1.4 \pm 0.5\%$ when $[Ca^{2+}]_o$ was reduced to 0.5 mM $[Ca^{2+}]_o$ ($n = 5$, FOV = 6). Ca^{2+} transients in cell processes were reduced in a similar manner upon reduction of $[Ca^{2+}]_o$ (Fig. 6 F). Under control conditions, the probability of Ca^{2+} site firing during a CTC was $65.7 \pm 1.6\%$, and the probability was reduced to $18.2 \pm 1.3\%$ and $5.8 \pm 0.9\%$ when $[Ca^{2+}]_o$ was reduced to 1 mM and 0.5 mM, respectively ($n = 5$, FOV = 6). In cell somata and processes, the probability of firing during a CTC was significantly reduced at all reduced concentrations of $[Ca^{2+}]_o$ tested ($P < 0.05$, $n = 5$, FOV = 6), and complete removal of Ca^{2+} from the bath abolished all Ca^{2+} signals. Concentration–response relationships for the effects of reduced $[Ca^{2+}]_o$ on the parameters described are shown in Table 1.

L-type Ca^{2+} channels are not a major factor in the generation of ICC-MY CTCs

The sequence of slow wave depolarization before activation of CTCs and the dependence of Ca^{2+} transients on $[Ca^{2+}]_o$ suggest that the mechanism for entraining CTCs involves voltage-dependent Ca^{2+} entry. ICC-MY express voltage-dependent Ca^{2+} channels (see Fig. S1), and T-type currents are elicited by depolarization and are important for slow waves in these cells (Zheng et al., 2014). The slow waves recorded in the present study were propagated events, and previous studies have also shown that slow wave propagation velocity and upstroke velocity are reduced or blocked in response to T-channel antagonists (Bayguinov et al., 2007; Zheng et al., 2014). In contrast, many studies have shown

that slow waves are resistant to dihydropyridines, suggesting that $Ca_V1.2$ channels are not involved in slow waves (Ozaki et al., 1991; Ward et al., 1994; Malysz et al., 2001; Kito et al., 2005; Park et al., 2006; Lee et al., 2007; Singh et al., 2014).

We used 100 nM nicardipine in the present study to reduce tissue movement. To investigate whether L-type Ca^{2+} channels contribute to CTCs, the concentration of nicardipine was increased in some experiments. Increasing nicardipine to 1 µM had no effect on CTC parameters (e.g., number of Ca^{2+} firing sites, firing probabilities, or PTCL area or counts; Fig. S2, $n = 5$, FOV = 7). However, higher concentrations of nicardipine (3 µM) affected CTCs (e.g., PTCL area in the somata and the processes were reduced by 45% and 58%, respectively; Table S1, $n = 5$, FOV = 7).

The experiments above rule out a role for Cav 1.2 (Cacna1c) channels in CTCs, but ICC-MY also express $Ca_V1.3$ (Cacna1d; Fig. S1), and the contribution of these channels in CTCs was also investigated. 1 µM isradipine, a blocker of $Ca_V1.2$ and $Ca_V1.3$, had no significant effects on CTCs (Fig. S3, $n = 4$, FOV = 4).

T-type Ca^{2+} channels contribution to the generation of ICC-MY CTCs

Previous studies showed that Ni^{2+} (>100 µM) or mibefradil (30 µM) inhibits slow waves in the small intestine, leading the authors to suggest that Ca^{2+} influx via T-type Ca^{2+} channels may be involved in slow wave propagation (Kito and Suzuki, 2003; Kito et al., 2005, 2015). We examined the role of a T-type conductance in slow waves and CTCs using NNC 55-0396 and TTA-A2. These new generation blockers are more specific than Ni^{2+} or mibefradil for T-type Ca^{2+} channels and do not produce metabolites that inhibit other channels (Huang et al., 2004; Kraus et al., 2010). NNC 55-0396 (500 nM; $n = 5$) did not affect slow wave amplitude, frequency, duration, dV/dt, or resting membrane potential (Fig. S4); however, at 1 µM, NNC 55-0396 reduced dV/dt and amplitude (Fig. S4 E and Fig. 4 H, both $P < 0.01$, $n = 5$). The same concentration of TTA-A2 significantly inhibited slow wave frequency (Fig. S4 N, $P < 0.05$, $n = 6$) and dV/dt (Fig. S4 P, $P < 0.05$, $n = 6$). Higher concentrations of these blockers further reduced slow waves, but also had effects on resting membrane potentials, suggesting possible nonspecific effects.

Although previous studies (Huang et al., 2004; Kraus et al., 2010) have verified the effectiveness of NNC 55-0396 and TTA-A2 on different classes of T-channels, we tested these compounds on the major class of T-channels expressed in ICC-MY ($Ca_V3.2$; Fig. S1 B) that were expressed homologously in HEK293 cells. TTA-A2 (1 µM) inhibited $Ca_V3.2$ currents by 78% at -40 mV, and NNC 55-0396 (1 µM) had similar effects, blocking the current by 85.1% at -40 mV (Fig. S5). These results confirm the effectiveness of the T-type channel antagonists.

ICC Ca^{2+} transient clustering | Drumm et al.

We tested the effects of NNC 55-0396 (1 µM) and TTA-A2 (1 µM) on CTCs. NNC 55-0396 significantly inhibited CTCs (Fig. 7, A and B). PTCL count and PTCL area traces (Fig. 7 C) describe the inhibitory effects of NNC 55-0396 on CTCs. This compound also reduced the probability of Ca^{2+} site firing in cell somata (54% in control and $5.1 \pm 1.3\%$ in the presence of NNC 55-0396; Fig. 7 D) and processes (Fig. 7 E; 49.2 ± 1.5 in control to $8.3 \pm 1\%$ in the presence of NNC 55-0396; both P < 0.0001, $n = 6$, FOV = 8). NNC 55-0396 also inhibited the number of firing sites, total PTCL area, and number of PTCLs in cell somata and processes (Fig. 7, F–K).

TTA-A2 also inhibited CTCs (Fig. 8, A and B). PTCL count and PTCL area traces described the inhibitory effects of TTA-A2 on CTCs (Fig. 8 C). This compound also reduced the probability of Ca^{2+} site firing in cell somata ($48.4 \pm 2.9\%$ in control and $1.3 \pm 0.4\%$ in the presence of TTA-A2; Fig. 8 D) and processes (Fig. 8 E; $44.6 \pm 1.57\%$ in control to $5.1 \pm 0.8\%$ in the presence of TTA-A2; both P < 0.0001, $n = 5$, FOV = 6). TTA-A2 also inhibited the number of firing sites, total PTCL area, and number of PTCLs in cell somata and processes (Fig. 8, F–K).

Role of intracellular Ca^{2+} stores in the generation of Ca^{2+} transients

Depolarization activates transient Ca^{2+} entry via T-type channels (Nowycky et al., 1985), and it is unlikely that the asynchronous CTCs firing throughout slow waves in ICC-MY were due solely to Ca^{2+} influx via these channels. Previous studies reported inhibitory effects of Ca^{2+}-store drugs on slow waves and the Ano1 currents that contribute to these events (Malysz et al., 2001; Ward et al., 2003; Bayguinov et al., 2007; Kito et al., 2015; Zhu et al., 2015). Therefore, we tested whether Ca^{2+} release mechanisms are involved in the generation of CTCs.

Thapsigargin (10 µM), a sarco/endoplasmic Ca^{2+}-ATPase (SERCA) pump antagonist, inhibited CTCs, rendering complete block of these events (Fig. 9, A and B). PTCL count and PTCL area traces show the inhibitory effects of thapsigargin on ICC-MY CTCs (Fig. 9 C). In control conditions, the firing probability of Ca^{2+} sites was $64.9 \pm 3\%$ in cell somata and $59 \pm 1.8\%$ in cell processes, and the firing sites per cell soma and processes were 3.71 ± 0.66 and 37.4 ± 7.7, respectively. PTCL area and PTCL count in the cell soma were 35.6 ± 6.7 µm^2 and 1.2 ± 0.2, respectively. PTCL area and count in the cell processes were 93.9 ± 22.75 µm^2 and 2.62 ± 0.27, respectively. Thapsigargin abolished CTCs and the effects were statistically significant in all cases (Fig. 9, D–K, $n = 5$, FOV = 5).

Contribution of RyR and IP$_3$ receptors (IP$_3$Rs) in the generation of CTCs in ICC-MY

Ryanodine (100 µM) either abolished (three/five experiments) or significantly reduced CTCs in ICC-MY

(Fig. 10 A). Occurrence maps (Fig. 10 B) and PTCL count and PTCL area traces (Fig. 10 C) also demonstrate the inhibitory effects of ryanodine on CTCs. The firing probability of Ca^{2+} release sites in cell somata decreased from $74.1 \pm 1.7\%$ in control to $2.5 \pm 0.4\%$ in the presence of ryanodine (P < 0.0001, $n = 5$, FOV = 5). Firing probability also decreased in cell processes from $66.4 \pm 1.4\%$ in control to $0.9 \pm 0.3\%$ in ryanodine (Fig. 10 E, P < 0.0001, $n = 5$, FOV = 5). The number of firing sites, total PTCL area, and number of PTCLs in cell somata and processes were also significantly inhibited by ryanodine (Fig. 10, F–K).

10 µM XeC did not have dramatic effects on CTCs in ICC-MY (Fig. 11 A). In the presence of XeC, ICC-MY persisted to generate CTCs, and these events were organized into rhythmic cycles as in control. No significant changes were noted in response to XeC in occurrence (Fig. 11 B) or in PTCL count and PTCL area traces (Fig. 11 C). The number of Ca^{2+} firing sites per cell soma was not changed significantly (3.7 ± 0.3 in control to 4.1 ± 0.5 in XeC; Fig. 11 F, P = 0.25, $n = 3$, FOV = 3) or in cell processes (66.3 ± 3.7 in control to 68 ± 22.1 in XeC; Fig. 11 E, P = 0.93, $n = 3$, FOV = 3) by XeC. The number of firing sites, total PTCL area, and number of PTCLs per frame in cell somata and processes were not significantly affected by XeC (Fig. 11, F–K).

In spite of the lack of dramatic effects of XeC, a significant difference was found in the probability of Ca^{2+} firing in cell somata and processes. The probability of Ca^{2+} release from firing sites during CTCs averaged $78.9 \pm 2.4\%$ in cell somata and XeC reduced the Ca^{2+} release probability to $68.4 \pm 1.9\%$ (Fig. 11 D, P = 0.006, $n = 3$, FOV = 3). Similar effects were noted in cell processes in which the mean probability of Ca^{2+} release from firing sites was $71.1 \pm 1.8\%$ during control and $62.7 \pm 1.3\%$ in the presence of XeC (Fig. 11 E, P < 0.0001, $n = 3$, FOV = 3).

DISCUSSION

In this study, we monitored Ca^{2+} transients in ICC-MY in situ using a genetically encoded Ca^{2+} biosensor (GCaMP3), and we were able to resolve subcellular Ca^{2+} transients that were seen only as global Ca^{2+} waves in previous studies (Park et al., 2006; Lee et al., 2007). Ca^{2+} signaling during propagating slow waves was examined; we never observed the fundamental pacemaker events that initiated the slow waves. In the intact tissue preparations we used, slow waves were initiated outside the FOV and actively propagated to the FOV under observation. Active propagation of slow waves included upstroke depolarization followed by initiation of CTCs. Slow waves depend on Ca^{2+}-activated Cl$^-$ channels encoded by *Ano1* (Hwang et al., 2009; Zhu et al., 2009). Activation of Ano1 channels requires elevation in $[Ca^{2+}]_i$, and how that is accomplished
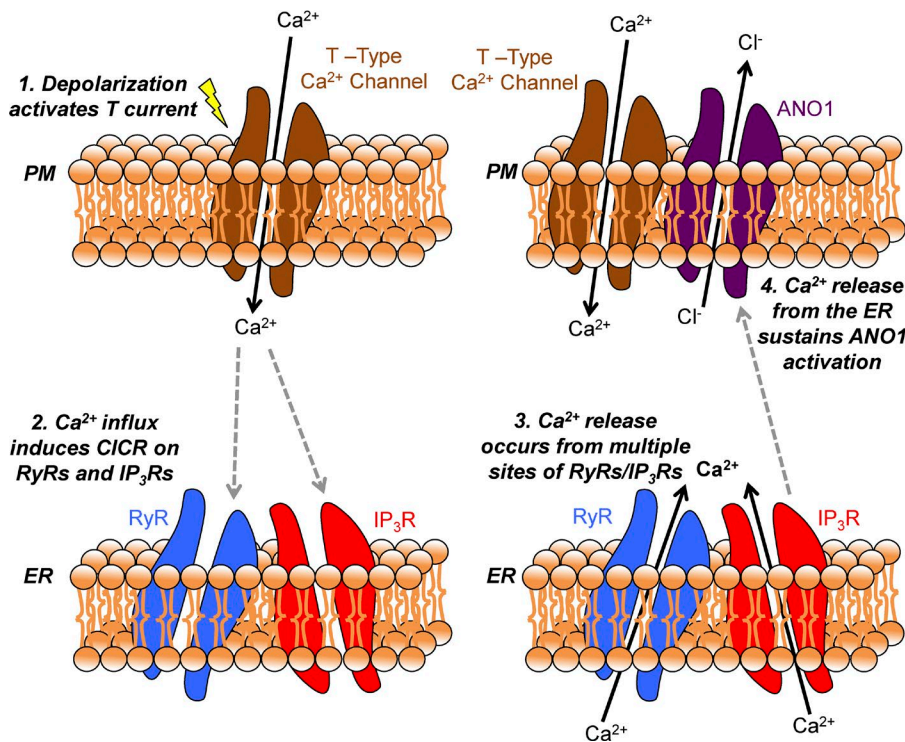
Propagation of slow waves

Figure 12. **Mechanism of slow wave propagation via asynchronous Ca^{2+} release.** Schematic showing the mechanism by which slow waves in the mouse small intestine propagate via asynchronous ER Ca^{2+} release. Electrical slow waves are propagating depolarizing events, which are actively propagated through ICC-MY networks. (1) When a slow wave propagates through the ICC-MY network, the resulting depolarization activates voltage-gated T-type Ca^{2+} channels on the plasma membrane. (2) Ca^{2+} influx from the opening of T-type Ca^{2+} channels allows Ca^{2+} ions to enter an excluded volume or microdomain and can then activate Ca^{2+} release channels such as RyRs (with amplification from IP$_3$Rs) on the membrane of the ER, possibly via a CICR mechanism. (3) Multiple sites of RyRs/IP$_3$Rs are located across multiple microdomains in a given single ICC-MY, and thus Ca^{2+} release occurs from multiple sites. Because of the excluded volume of the microdomain, individual Ca^{2+} release events manifests as temporally brief events that also occur asynchronously among each other, leading to a summated Ca^{2+} signal from the total sites in a cell lasting ~1 s. (4) The summated Ca^{2+} signal resulting from multiple Ca^{2+} release events is able to sustain ANO1 activation, resulting in prolonged Cl$^-$ efflux from the cell and a corresponding sustained depolarization for the duration of the slow wave plateau. RyR, ryanodine receptor; PM, plasma membrane; CICR, calcium-induced calcium release.

and sustained for the relatively long durations of slow waves (>1 s) was previously unknown. We were able to image Ca^{2+} transients with high signal-to-noise ratios in ICC-MY expressing GCaMP3. These experiments showed that Ca^{2+} transients do not occur in a stochastic manner in ICC-MY, as found in the intramuscular class of ICC (ICC-DMP) in the small intestine (Baker et al., 2016). Ca^{2+} transients were entrained by voltage-dependent Ca^{2+} entry into CTCs in ICC-MY. Depolarization during the slow wave plateau phase was approximately the same duration as the period of asynchronous of Ca^{2+} transients during CTCs. Ca^{2+} release sites in cell somata and in processes contributed to CTCs with similar firing probabilities. Localized Ca^{2+} release in ICC and dependence of CTCs on a T-type conductance, but not L-type conductances, which are also expressed in ICC-MY (Fig. S1), support the idea that Ca^{2+} microdomains are an important feature of the pacemaker mechanism, and T-type channels may be closely associated with Ca^{2+} release channels and Ano1 channels within these microdomains.

Ca^{2+} transients in ICC in relation to slow waves

Previous studies showed that electrical slow waves in mouse (Park et al., 2006) and human (Lee et al., 2007) GI muscles are associated with Ca^{2+} oscillations in ICC-MY networks. However, all previous studies of Ca^{2+} events in ICC-MY have been limited to the resolution of global Ca^{2+} measurements because of several factors, including loading efficiency of Ca^{2+} indicators, dye bleaching, low acquisition rates, and signal bleed-through from non-ICC cell types in surrounding muscle tissues. In the present study, Kit-Cre-GCaMP3 mice were used to enhance the resolution of Ca^{2+} transients in ICC-MY with higher magnification and acquisition rates. We attempted to impale ICC-MY during the course of imaging, but as yet we have failed to make direct recording from these cells while imaging Ca^{2+} transients. Slow waves conduct passively from ICC-MY to smooth muscle cells (Cousins et al., 2003), so the temporal relationship between cells imaged and slow waves recorded from impalements of nearby smooth muscle cells should not have been distorted excessively. When simultaneous recordings of

slow waves were made during imaging, temporal clustering of Ca^{2+} transients during the time-course of slow waves was noted. We found that the upstroke depolarizations of slow waves preceded the CTCs by ∼175 ms. These data suggest that the temporal clustering of Ca^{2+} release events during propagating slow waves is entrained by a voltage-dependent mechanism. This delay is consistent with a previous report (Park et al., 2006) although the lag time observed could be the result of several factors. In this study, we were unable to resolve/isolate calcium entry signals at the microdomains; therefore, we speculate that calcium entry mechanisms are activated during this lag time. Another explanation of the Ca^{2+} signal delay might be because they emerge from the portion of the tissue that is in view, whereas the electrical signal, coming from the syncytium, may have additional contributing current from dominant regions outside of the FOV.

Nature of the ICC-MY Ca^{2+} transients

The characteristics of CTCs in ICC-MY provide new information on how Ca^{2+} signaling contributes to slow wave duration and overall contractility. Imaging of muscles from Kit-Cre-GCaMP3 mice revealed the variable nature of Ca^{2+} transients in ICC-MY networks and at different sites within cells. The Ca^{2+} transients resolved into multiple, discrete events arising from many sites within cell somata and processes. ICC-MY displaying only a single firing site were extremely rare. Although some sites fired Ca^{2+} transients during every CTC, many did not, and the pattern of site firing could change significantly from one CTC cycle to the next. However, summation of CTCs from several cells within FOVs resulted in relatively consistent Ca^{2+} responses in the ICC-MY network cycle-to-cycle. Staggered Ca^{2+} transients occurring from many sites would tend to increase the period of Ano1 activation in ICC-MY, and thus the occurrence of CTCs appears to be the basis for the relatively long durations of slow waves.

Role of Ca^{2+} influx in ICC-MY Ca^{2+} transient firing

The rates of slow wave propagation and the Ca^{2+} waves associated with slow waves suggest a voltage-dependent mechanism for active propagation (Park et al., 2006; Bayguinov et al., 2007). The mechanism of the voltage-dependent step has been controversial, and voltage-dependent Ca^{2+} entry (Sanders et al., 2014) and voltage-dependent production of IP$_3$ have been posited (Hirst et al., 2002). To date, voltage-dependent production of IP$_3$ has not been demonstrated in ICC, whereas many studies have supported the idea that propagation of electrical slow waves depends on Ca^{2+} influx (Kito and Suzuki, 2003; Ward et al., 2003, 2004; Bayguinov et al., 2007; Kito et al., 2015). There is also previous support for the role of T-type Ca^{2+} channels in the propagation of slow waves because blockers of these channels reduce dV/dt of the upstroke depolarization,

reduce propagation rates in stomach (Ward et al., 2004; Bayguinov et al., 2007), small bowel (Kito and Suzuki, 2003; Kito et al., 2005, 2015), and colon (Ward et al., 2003), or abolish slow waves altogether. Furthermore, Ni^{2+} and mibefradil inhibited Ca^{2+} waves in ICC-MY in previous lower resolution imaging studies (Park et al., 2006; Lee et al., 2007). These studies are consistent with the current findings that clustering of Ca^{2+} transients in ICC-MY depends on Ca^{2+} influx. Reducing [Ca^{2+}]$_o$ decreased the probability of CTC firing and removal of Ca^{2+} from the extracellular solution abolished CTCs. The Ca^{2+} influx required for CTCs did not appear to occur via L-type Ca^{2+} channels as blockers of Cav1.2 and Cav1.3 channels failed to block CTCs.

Our hypothesis is that voltage-dependent Ca^{2+} entry entrains Ca^{2+} release events through Ca^{2+}-induced Ca^{2+} release to produce CTCs. Unfortunately, at present, we must leave this as a hypothesis because we have not yet been able to independently resolve the Ca^{2+} entry events in ICC-MY. The peak current attributed to a T-type Ca^{2+} conductance in ICC-MY was found to be ∼7 pA/pF (at −20 mV; Zheng et al., 2014). For such small currents to impact [Ca^{2+}]$_i$ effectively, these channels may be arranged into microdomains in close proximity to ER release channels. Other Ca^{2+} sources within these microdomains (e.g., a store operated conductance, Na$^+$/Ca^{2+} exchange) may sustain Ca^{2+} entry into microdomains to support sustained, asynchronous Ca^{2+} release events making up CTCs.

The firing patterns of ICC-MY contrast significantly with the Ca^{2+} release events in the second type of ICC in the small intestine, ICC within the deep muscular plexus (ICC-DMP). ICC-DMP display stochastic firing of Ca^{2+} transients that are independent of Ca^{2+} influx mechanisms (Baker et al., 2016). One explanation for the disparate firing patterns of ICC-MY and ICC-DMP might be the lack of a voltage-dependent mechanism to entrain Ca^{2+} release in ICC-DMP. Gene array studies showed that ICC-DMP have low expression of voltage-dependent Ca^{2+} channel genes (Chen et al., 2007), whereas ICC-MY express *Cacna1h*, a T-type conductance, and *Cacna1c* and *Cacna1d*, L-type conductances (Gibbons et al., 2009; Zheng et al., 2014). In the present study, T-type Ca^{2+} channel blockers, NNC 55-0396 and TTA-A2, prevented entrainment of Ca^{2+} release events in ICC-MY.

Ca^{2+} influx in ICC-MY may increase the sensitivity of Ca^{2+} release channels through cytosolic binding sites that increase the open probability of Ca^{2+} release channels or activate release channels directly by CICR (Berridge et al., 2000). Ca^{2+} influx may also raise ER [Ca^{2+}] past a critical threshold, activating luminal-binding sites within the ER and increasing Ca^{2+} release.

Ca^{2+} release leads to the Ca^{2+} transients in ICC-MY

Previous studies have shown that slow waves are reduced in frequency or abolished when intracellular

Ca^{2+} stores are disrupted in a range of GI tissues (Ward et al., 2003; Bayguinov et al., 2007; Lowie et al., 2011; Kito et al., 2015). Our findings also suggest that Ca^{2+} release from stores is the source for CTCs in ICC-MY. Thapsigargin, an inhibitor of the SERCA pump, completely abolished CTCs. This drug also abolished slow wave activity in intact murine small intestinal muscles (Malysz et al., 2001). ICC of the small intestine express *Ryr1-3* with *Ryr2* being the dominant transcript; *Itpr1* is the dominant IP$_3$R gene expressed (Baker et al., 2016). We investigated which class of Ca^{2+} release channels is responsible for CTCs associated with slow waves. Blocking RyRs with ryanodine caused near abolition of CTCs in ICC-MY. Ryanodine block of activity suggests that RyRs have an important role in generating CTCs in ICC-MY. Localized RyR-mediated Ca^{2+} events (Ca^{2+} sparks) present in cardiac and smooth muscle (Cheng et al., 1993; Nelson et al., 1995; Jaggar et al., 2000) have also been reported to initiate global Ca^{2+} waves in ICC from the rabbit urethra (Drumm et al., 2015). Because CTCs in ICC-MY depend up ryanodine receptors, it is likely that they originate as spark-like events. However, the events in ICC-MY have greater spatial and temporal characteristics than classical Ca^{2+} sparks, as described in cardiac cells (Cheng et al., 1993; Wier et al., 1997; Smith et al., 1998) as well as smooth muscle cells (ZhuGe et al., 1999; Curtis et al., 2004). In ICC-MY, sparks appear to be amplified by localized propagation via CICR or by additional Ca^{2+} release mechanisms, such as Ca^{2+} release from the IP$_3$Rs.

Previous studies that tested the role of RyRs found only a minor role for this pathway in slow waves, but these studies used concentrations of ryanodine (10–50 µM; Malysz et al., 2001; Park et al., 2006; Lee et al., 2007) that may have been too low to block RyR in intact tissues (Meissner, 1986; Serysheva, 1998; Bootman et al., 2001; Baker et al., 2016). Malysz et al. (2001) found that 50 µM ryanodine reduced slow wave amplitude and frequency in the mouse small intestine, but they attributed the effects to the depolarization caused by ryanodine in their experiments. Depolarization, however, is unlikely to account for the effects of ryanodine, as slow waves recorded under current clamp from isolated ICC from the mouse small intestine were also blocked by ryanodine (Zhu et al., 2015).

IP$_3$Rs also contribute to CTCs in ICC-MY. Although XeC did not significantly affect the number of Ca^{2+} release sites, it reduced the probability of Ca^{2+} release. Our data contrast with previous studies about the importance of IP$_3$Rs in slow waves (Malysz et al., 2001; Park et al., 2006; Lee et al., 2007). The major study suggesting the importance of IP$_3$Rs was a global knockout study in which slow waves were abolished in gastric muscles of *Itpr1*$^{-/-}$ mice (Suzuki et al., 2000). Differences in the relative importance of RyR and IP$_3$R might exist in different ICC networks and in different organs. For example,

we found inhibitory effects of XeC on Ca^{2+} transients in ICC-DMP of the small intestine (Baker et al., 2016), but the same effects were not observed in ICC-MY. It should also be noted that XeC has been reported to block ER store loading and have minimal effects on IP$_3$Rs (Saleem et al., 2014). Thus, off-target effects, which may account for the lack of effect of blocking IP$_3$Rs in the current study, cannot be excluded. The difficulties in using pharmacological agents to probe the intracellular Ca^{2+} machinery means that additional studies using ICC-specific inducible knockouts of specific paralogues of RyRs and IP$_3$Rs may be necessary.

The heterogeneity in firing patterns between CTCs could be caused by the Ca^{2+} events arising from a cluster of Ca^{2+} release channels acting in concert. This may be explained by variable numbers of receptors in each cluster, and the open probability of receptors within each cluster may change from one CTC to the next, depending on factors such as SR Ca^{2+} loading and cytosolic Ca^{2+} levels, which might affect Ca^{2+} release and explain the variability in Ca^{2+} transients making up CTCs (e.g., firing patterns, numbers of firing sites, and spatial variations; González et al., 2000; Wellman and Nelson, 2003; Gordienko et al., 2004; Wang et al., 2004; ZhuGe et al., 2004).

In conclusion, activation of Ano1 channels that participate in slow waves in ICC-MY depend on a Ca^{2+} source that is sustained during the duration of the plateau phase of slow waves (Sanders et al., 2014; Cabrita et al., 2017). In this study, we solely examined Ca^{2+} signals in ICC-MY during the propagating phase of slow waves. Although we currently do not have direct evidence of the Ca^{2+} initiation phase of slow waves, we found that Ca^{2+} transients occurring during the plateau phase of propagating slow waves are largely caused by the release of Ca^{2+} from stores via RyR receptors. Voltage-dependent Ca^{2+} entry entrains Ca^{2+} release events into CTCs. The upstrokes of propagating slow waves, recorded in close proximity to the cells being imaged, slightly preceded the onset of the CTCs. Data from the present study and previous studies (Zheng et al., 2014) have suggested that Ca^{2+} entry occurs through a T-type Ca^{2+} conductance. Currents through T-type channels in ICC are small, and this, together with the localized nature of Ca^{2+} transients ICC-MY, suggests that Ca^{2+} entry and release from intracellular stores may occur in specialized microdomains. Ca^{2+} release events within CTCs occur asynchronously from multiple sites, and these events appear to define the duration of the slow wave plateau. A summary diagram detailing this mechanism is shown in Fig. 12. Because depolarization during the plateau potential initiates Ca^{2+} action potentials in smooth muscle cells and excitation-contraction coupling, the dynamics and characteristics of Ca^{2+} transients in ICC-MY must be considered a fundamental mechanism responsible for GI motor function.

REFERENCES

Baker, S.A., G.W. Hennig, A.K. Salter, M. Kurahashi, S.M. Ward, and K.M. Sanders. 2013. Distribution and Ca^{2+} signalling of fibroblast-like (PDGFRα$^+$) cells in the murine gastric fundus. *J. Physiol.* 591:6193–6208. http://dx.doi.org/10.1113/jphysiol.2013.264747

Baker, S.A., G.W. Hennig, S.M. Ward, and K.M. Sanders. 2015. Temporal sequence of activation of cells involved in purinergic neurotransmission in the colon. *J. Physiol.* 593:1945–1963. http://dx.doi.org/10.1113/jphysiol.2014.287599

Baker, S.A., B.T. Drumm, D. Saur, G.W. Hennig, S.M. Ward, and K.M. Sanders. 2016. Spontaneous Ca^{2+} transients in interstitial cells of Cajal located within the deep muscular plexus of the murine small intestine. *J. Physiol.* 594:3317–3338. http://dx.doi.org/10.1113/JP271699

Bayguinov, O., S.M. Ward, J.L. Kenyon, and K.M. Sanders. 2007. Voltage-gated Ca^{2+} currents are necessary for slow-wave propagation in the canine gastric antrum. *Am. J. Physiol. Cell Physiol.* 293:C1645–C1659. http://dx.doi.org/10.1152/ajpcell.00165.2007

Berridge, M.J., P. Lipp, and M.D. Bootman. 2000. The versatility and universality of calcium signalling. *Nat. Rev. Mol. Cell Biol.* 1:11–21. http://dx.doi.org/10.1038/35036035

Bootman, M.D., T.J. Collins, C.M. Peppiatt, L.S. Prothero, L. MacKenzie, P. De Smet, M. Travers, S.C. Tovey, J.T. Seo, M.J. Berridge, et al. 2001. Calcium signalling–an overview. *Semin. Cell Dev. Biol.* 12:3–10. http://dx.doi.org/10.1006/scdb.2000.0211

Burns, A.J., A.E. Lomax, S. Torihashi, K.M. Sanders, and S.M. Ward. 1996. Interstitial cells of Cajal mediate inhibitory neurotransmission in the stomach. *Proc. Natl. Acad. Sci. USA.* 93:12008–12013. http://dx.doi.org/10.1073/pnas.93.21.12008

Burnstock, G., M.E. Holman, and C.L. Prosser. 1963. Electrophysiology of smooth muscle. *Physiol. Rev.* 43:482–527.

Cabrita, I., R. Benedetto, A. Fonseca, P. Wanitchakool, L. Sirianant, B.V. Skryabin, L.K. Schenk, H. Pavenstädt, R. Schreiber, and K. Kunzelmann. 2017. Differential effects of anoctamins on intracellular calcium signals. *FASEB J.* 31:2123–2134. http://dx.doi.org/10.1096/fj.201600797RR

Chen, H., T. Ördög, J. Chen, D.L. Young, M.R. Bardsley, D. Redelman, S.M. Ward, and K.M. Sanders. 2007. Differential gene expression in functional classes of interstitial cells of Cajal in murine small intestine. *Physiol. Genomics.* 31:492–509. http://dx.doi.org/10.1152/physiolgenomics.00113.2007

Cheng, H., W.J. Lederer, and M.B. Cannell. 1993. Calcium sparks: elementary events underlying excitation-contraction coupling in heart muscle. *Science.* 262:740–744. http://dx.doi.org/10.1126/science.8235594

Cousins, H.M., F.R. Edwards, H. Hickey, C.E. Hill, and G.D. Hirst. 2003. Electrical coupling between the myenteric interstitial cells of Cajal and adjacent muscle layers in the guinea-pig gastric antrum. *J. Physiol.* 550:829–844. http://dx.doi.org/10.1113/jphysiol.2003.042176

Curtis, T.M., J. Tumelty, J. Dawicki, C.N. Scholfield, and J.G. McGeown. 2004. Identification and spatiotemporal characterization of spontaneous Ca^{2+} sparks and global Ca^{2+} oscillations in retinal arteriolar smooth muscle cells. *Invest. Ophthalmol. Vis. Sci.* 45:4409–4414. http://dx.doi.org/10.1167/iovs.04-0719

Dickens, E.J., G.D. Hirst, and T. Tomita. 1999. Identification of rhythmically active cells in guinea-pig stomach. *J. Physiol.* 514:515–531. http://dx.doi.org/10.1111/j.1469-7793.1999.515ae.x

Drumm, B.T., R.J. Large, M.A. Hollywood, K.D. Thornbury, S.A. Baker, B.J. Harvey, N.G. McHale, and G.P. Sergeant. 2015. The role of Ca^{2+} influx in spontaneous Ca^{2+} wave propagation in interstitial cells of Cajal from the rabbit urethra. *J. Physiol.* 593:3333–3350. http://dx.doi.org/10.1113/JP270883

Gibbons, S.J., P.R. Strege, S. Lei, J.L. Roeder, A. Mazzone, Y. Ou, A. Rich, and G. Farrugia. 2009. The α$_{1H}$ Ca^{2+} channel subunit is expressed in mouse jejunal interstitial cells of Cajal and myocytes. *J. Cell. Mol. Med.* 13:4422–4431. http://dx.doi.org/10.1111/j.1582-4934.2008.00623.x

González, A., W.G. Kirsch, N. Shirokova, G. Pizarro, G. Brum, I.N. Pessah, M.D. Stern, H. Cheng, and E. Ríos. 2000. Involvement of multiple intracellular release channels in calcium sparks of skeletal muscle. *Proc. Natl. Acad. Sci. USA.* 97:4380–4385. http://dx.doi.org/10.1073/pnas.070056497

Gordienko, D.V., A.V. Zholos, M.F. Shuba, and T.B. Bolton. 2004. Mechanisms of calcium signalling in smooth muscle cells explored with fluorescence confocal imaging. *Neurophysiology.* 36:407–417. http://dx.doi.org/10.1007/s11062-005-0035-1

Hirst, G.D., N.J. Bramich, N. Teramoto, H. Suzuki, and F.R. Edwards. 2002. Regenerative component of slow waves in the guinea-pig gastric antrum involves a delayed increase in $[Ca^{2+}]_i$ and Cl$^-$ channels. *J. Physiol.* 540:907–919. http://dx.doi.org/10.1113/jphysiol.2001.014803

Huang, L., B.M. Keyser, T.M. Tagmose, J.B. Hansen, J.T. Taylor, H. Zhuang, M. Zhang, D.S. Ragsdale, and M. Li. 2004. NNC 55-0396 [(1S,2S)-2-(2-(N-[(3-benzimidazol-2-yl)propyl]-N-methylamino)ethyl)-6-fluoro-1,2,3,4-tetrahydro-1-isopropyl-2-naphtyl cyclopropanecarboxylate dihydrochloride]: a new selective inhibitor of T-type calcium channels. *J. Pharmacol. Exp. Ther.* 309:193–199. http://dx.doi.org/10.1124/jpet.103.060814

Huizinga, J.D., L. Thuneberg, M. Klüppel, J. Malysz, H.B. Mikkelsen, and A. Bernstein. 1995. *W/kit* gene required for interstitial cells of Cajal and for intestinal pacemaker activity. *Nature.* 373:347–349. http://dx.doi.org/10.1038/373347a0

Hwang, S.J., P.J. Blair, F.C. Britton, K.E. O'Driscoll, G. Hennig, Y.R. Bayguinov, J.R. Rock, B.D. Harfe, K.M. Sanders, and S.M. Ward. 2009. Expression of anoctamin 1/TMEM16A by interstitial cells of Cajal is fundamental for slow wave activity in gastrointestinal muscles. *J. Physiol.* 587:4887–4904. http://dx.doi.org/10.1113/jphysiol.2009.176198

Iwasaki, H., Y. Mori, Y. Hara, K. Uchida, H. Zhou, and K. Mikoshiba. 2001. 2-Aminoethoxydiphenyl borate (2-APB) inhibits capacitative calcium entry independently of the function of inositol 1,4,5-trisphosphate receptors. *Receptors Channels.* 7:429–439.

Jaggar, J.H., V.A. Porter, W.J. Lederer, and M.T. Nelson. 2000. Calcium sparks in smooth muscle. *Am. J. Physiol. Cell Physiol.* 278:C235–C256.

Kito, Y., and H. Suzuki. 2003. Properties of pacemaker potentials recorded from myenteric interstitial cells of Cajal distributed in the mouse small intestine. *J. Physiol.* 553:803–818. http://dx.doi.org/10.1113/jphysiol.2003.051334

Kito, Y., S.M. Ward, and K.M. Sanders. 2005. Pacemaker potentials generated by interstitial cells of Cajal in the murine intestine. *Am. J. Physiol. Cell Physiol.* 288:C710–C720. http://dx.doi.org/10.1152/ajpcell.00361.2004

Kito, Y., R. Mitsui, S.M. Ward, and K.M. Sanders. 2015. Characterization of slow waves generated by myenteric interstitial cells of Cajal of the rabbit small intestine. *Am. J. Physiol. Gastrointest. Liver Physiol.* 308:G378–G388. http://dx.doi.org/10.1152/ajpgi.00308.2014

Komuro, T. 2006. Structure and organization of interstitial cells of Cajal in the gastrointestinal tract. *J. Physiol.* 576:653–658. http://dx.doi.org/10.1113/jphysiol.2006.116624

Kraus, R.L., Y. Li, Y. Gregan, A.L. Gotter, V.N. Uebele, S.V. Fox, S.M. Doran, J.C. Barrow, Z.Q. Yang, T.S. Reger, et al. 2010. In vitro characterization of T-type calcium channel antagonist TTA-A2 and in vivo effects on arousal in mice. *J. Pharmacol. Exp. Ther.* 335:409–417. http://dx.doi.org/10.1124/jpet.110.171058

Langton, P., S.M. Ward, A. Carl, M.A. Norell, and K.M. Sanders. 1989. Spontaneous electrical activity of interstitial cells of Cajal isolated from canine proximal colon. *Proc. Natl. Acad. Sci. USA.* 86:7280–7284. http://dx.doi.org/10.1073/pnas.86.18.7280

Lee, H.T., G.W. Hennig, N.W. Fleming, K.D. Keef, N.J. Spencer, S.M. Ward, K.M. Sanders, and T.K. Smith. 2007. The mechanism and spread of pacemaker activity through myenteric interstitial cells of Cajal in human small intestine. *Gastroenterology.* 132:1852–1865. http://dx.doi.org/10.1053/j.gastro.2007.02.049

Lowie, B.J., X.Y. Wang, E.J. White, and J.D. Huizinga. 2011. On the origin of rhythmic calcium transients in the ICC-MP of the mouse small intestine. *Am. J. Physiol. Gastrointest. Liver Physiol.* 301:G835–G845. http://dx.doi.org/10.1152/ajpgi.00077.2011

Malysz, J., G. Donnelly, and J.D. Huizinga. 2001. Regulation of slow wave frequency by IP$_3$-sensitive calcium release in the murine small intestine. *Am. J. Physiol. Gastrointest. Liver Physiol.* 280:G439–G448.

Meissner, G. 1986. Ryanodine activation and inhibition of the Ca^{2+} release channel of sarcoplasmic reticulum. *J. Biol. Chem.* 261:6300–6306.

Nelson, M.T., H. Cheng, M. Rubart, L.F. Santana, A.D. Bonev, H.J. Knot, and W.J. Lederer. 1995. Relaxation of arterial smooth muscle by calcium sparks. *Science.* 270:633–637. http://dx.doi.org/10.1126/science.270.5236.633

Nowycky, M.C., A.P. Fox, and R.W. Tsien. 1985. Three types of neuronal calcium channel with different calcium agonist sensitivity. *Nature.* 316:440–443. http://dx.doi.org/10.1038/316440a0

Ördög, T., S.M. Ward, and K.M. Sanders. 1999. Interstitial cells of cajal generate electrical slow waves in the murine stomach. *J. Physiol.* 518:257–269. http://dx.doi.org/10.1111/j.1469-7793.1999.0257r.x

Ördög, T., I. Takayama, W.K. Cheung, S.M. Ward, and K.M. Sanders. 2000. Remodeling of networks of interstitial cells of Cajal in a murine model of diabetic gastroparesis. *Diabetes.* 49:1731–1739. http://dx.doi.org/10.2337/diabetes.49.10.1731

Ozaki, H., R.J. Stevens, D.P. Blondfield, N.G. Publicover, and K.M. Sanders. 1991. Simultaneous measurement of membrane potential, cytosolic Ca^{2+}, and tension in intact smooth muscles. *Am. J. Physiol.* 260:C917–C925.

Park, K.J., G.W. Hennig, H.T. Lee, N.J. Spencer, S.M. Ward, T.K. Smith, and K.M. Sanders. 2006. Spatial and temporal mapping of pacemaker activity in interstitial cells of Cajal in mouse ileum in situ. *Am. J. Physiol. Cell Physiol.* 290:C1411–C1427. http://dx.doi.org/10.1152/ajpcell.00447.2005

Ro, S., C. Park, J. Jin, H. Zheng, P.J. Blair, D. Redelman, S.M. Ward, W. Yan, and K.M. Sanders. 2010. A model to study the phenotypic changes of interstitial cells of Cajal in gastrointestinal diseases. *Gastroenterology.* 138:1068–1078.e2. http://dx.doi.org/10.1053/j.gastro.2009.11.007

Saleem, H., S.C. Tovey, T.F. Molinski, and C.W. Taylor. 2014. Interactions of antagonists with subtypes of inositol 1,4,5-trisphosphate (IP3) receptor. *Br. J. Pharmacol.* 171:3298–3312. http://dx.doi.org/10.1111/bph.12685

Sanders, K.M., S.M. Ward, and S.D. Koh. 2014. Interstitial cells: regulators of smooth muscle function. *Physiol. Rev.* 94:859–907. http://dx.doi.org/10.1152/physrev.00037.2013

Serysheva, H.S. II. 1998. Ryanodine binding sites on the sarcoplasmic reticulum Ca^{2+} release channel. *In* Structure and Function of Ryanodine Receptors. R. Sitsapesan, and A.J. Williams, editors. Imperial College Press, London. 95–104. http://dx.doi.org/10.1142/9781848160538_0006

Singh, R.D., S.J. Gibbons, S.A. Saravanaperumal, P. Du, G.W. Hennig, S.T. Eisenman, A. Mazzone, Y. Hayashi, C. Cao, G.J. Stoltz, et al. 2014. Ano1, a Ca^{2+}-activated Cl$^-$ channel, coordinates contractility in mouse intestine by Ca^{2+} transient coordination between interstitial cells of Cajal. *J. Physiol.* 592:4051–4068. http://dx.doi.org/10.1113/jphysiol.2014.277152

Smith, G.D., J.E. Keizer, M.D. Stern, W.J. Lederer, and H. Cheng. 1998. A simple numerical model of calcium spark formation and detection in cardiac myocytes. *Biophys. J.* 75:15–32. http://dx.doi.org/10.1016/S0006-3495(98)77491-0

Suzuki, H, H Takano, Y Yamamoto, T Komuro, M Saito, K Kato, and K Mikoshiba. 2000. Properties of gastric smooth muscles obtained from mice which lack inositol trisphosphate receptor. *J Physiol.* 525:105–111.

Torihashi, S., S.M. Ward, S. Nishikawa, K. Nishi, S. Kobayashi, and K.M. Sanders. 1995. c-kit-dependent development of interstitial cells and electrical activity in the murine gastrointestinal tract. *Cell Tissue Res.* 280:97–111.

Wang, S.Q., M.D. Stern, E. Ríos, and H. Cheng. 2004. The quantal nature of Ca^{2+} sparks and *in situ* operation of the ryanodine receptor array in cardiac cells. *Proc. Natl. Acad. Sci. USA.* 101:3979–3984. http://dx.doi.org/10.1073/pnas.0306157101

Wang, X.Y., J.D. Huizinga, J. Diamond, and L.W. Liu. 2009. Loss of intramuscular and submuscular interstitial cells of Cajal and associated enteric nerves is related to decreased gastric emptying in streptozotocin-induced diabetes. *Neurogastroenterol. Motil.* 21:1095–e92. http://dx.doi.org/10.1111/j.1365-2982.2009.01336.x

Ward, S.M., A.J. Burns, S. Torihashi, and K.M. Sanders. 1994. Mutation of the proto-oncogene c-kit blocks development of interstitial cells and electrical rhythmicity in murine intestine. *J. Physiol.* 480:91–97. http://dx.doi.org/10.1113/jphysiol.1994.sp020343

Ward, S.M., T. Ördög, S.D. Koh, S.A. Baker, J.Y. Jun, G. Amberg, K. Monaghan, and K.M. Sanders. 2000. Pacemaking in interstitial cells of Cajal depends upon calcium handling by endoplasmic reticulum and mitochondria. *J. Physiol.* 525:355–361. http://dx.doi.org/10.1111/j.1469-7793.2000.t01-1-00355.x

Ward, S.M., S.A. Baker, A. de Faoite, and K.M. Sanders. 2003. Propagation of slow waves requires IP$_3$ receptors and mitochondrial Ca^{2+} uptake in canine colonic muscles. *J. Physiol.* 549:207–218. http://dx.doi.org/10.1113/jphysiol.2003.040097

Ward, S.M., R.E. Dixon, A. de Faoite, and K.M. Sanders. 2004. Voltage-dependent calcium entry underlies propagation of slow waves in canine gastric antrum. *J. Physiol.* 561:793–810. http://dx.doi.org/10.1113/jphysiol.2004.076067

Wellman, G.C., and M.T. Nelson. 2003. Signaling between SR and plasmalemma in smooth muscle: sparks and the activation of Ca^{2+}-sensitive ion channels. *Cell Calcium.* 34:211–229. http://dx.doi.org/10.1016/S0143-4160(03)00124-6

Wier, W.G., H.E. ter Keurs, E. Marban, W.D. Gao, and C.W. Balke. 1997. Ca^{2+} 'sparks' and waves in intact ventricular muscle resolved by confocal imaging. *Circ. Res.* 81:462–469. http://dx.doi.org/10.1161/01.RES.81.4.462

Winbush, A., M. Gruner, G.W. Hennig, and A.M. van der Linden. 2015. Long-term imaging of circadian locomotor rhythms of a freely crawling *C. elegans* population. *J. Neurosci. Methods.* 249:66–74. http://dx.doi.org/10.1016/j.jneumeth.2015.04.009

Won, K.J., K.M. Sanders, and S.M. Ward. 2005. Interstitial cells of Cajal mediate mechanosensitive responses in the stomach. *Proc. Natl. Acad. Sci. USA.* 102:14913–14918. http://dx.doi.org/10.1073/pnas.0503628102

Xu, W., and D. Lipscombe. 2001. Neuronal $Ca_V 1.3\alpha_1$ L-type channels activate at relatively hyperpolarized membrane potentials and are incompletely inhibited by dihydropyridines. *J. Neurosci.* 21:5944–5951.

Yamamoto, T., K. Watabe, M. Nakahara, H. Ogiyama, T. Kiyohara, S. Tsutsui, S. Tamura, Y. Shinomura, and N. Hayashi. 2008. Disturbed gastrointestinal motility and decreased interstitial cells of Cajal in diabetic db/db mice. *J. Gastroenterol. Hepatol.* 23:660–667. http://dx.doi.org/10.1111/j.1440-1746.2008.05326.x

Zheng, H., K.S. Park, S.D. Koh, and K.M. Sanders. 2014. Expression and function of a T-type Ca^{2+} conductance in interstitial cells of Cajal of the murine small intestine. *Am. J. Physiol. Cell Physiol.* 306:C705–C713. http://dx.doi.org/10.1152/ajpcell.00390.2013

Zhu, M.H., T.W. Kim, S. Ro, W. Yan, S.M. Ward, S.D. Koh, and K.M. Sanders. 2009. A Ca^{2+}-activated Cl^- conductance in interstitial cells of Cajal linked to slow wave currents and pacemaker activity. *J. Physiol.* 587:4905–4918. http://dx.doi.org/10.1113/jphysiol.2009.176206

Zhu, M.H., I.K. Sung, H. Zheng, T.S. Sung, F.C. Britton, K. O'Driscoll, S.D. Koh, and K.M. Sanders. 2011. Muscarinic activation of Ca^{2+}-activated Cl^- current in interstitial cells of Cajal. *J. Physiol.* 589:4565–4582. http://dx.doi.org/10.1113/jphysiol.2011.211094

Zhu, M.H., T.S. Sung, K. O'Driscoll, S.D. Koh, and K.M. Sanders. 2015. Intracellular Ca^{2+} release from endoplasmic reticulum regulates slow wave currents and pacemaker activity of interstitial cells of Cajal. *Am. J. Physiol. Cell Physiol.* 308:C608–C620. http://dx.doi.org/10.1152/ajpcell.00360.2014

Zhu, M.H., T.S. Sung, M. Kurahashi, L.E. O'Kane, K. O'Driscoll, S.D. Koh, and K.M. Sanders. 2016. Na^+-K^+-Cl^- cotransporter (NKCC) maintains the chloride gradient to sustain pacemaker activity in interstitial cells of Cajal. *Am. J. Physiol. Gastrointest. Liver Physiol.* 311:G1037–G1046. http://dx.doi.org/10.1152/ajpgi.00277.2016

ZhuGe, R., R.A. Tuft, K.E. Fogarty, K. Bellve, F.S. Fay, and J.V. Walsh Jr. 1999. The influence of sarcoplasmic reticulum Ca^{2+} concentration on Ca^{2+} sparks and spontaneous transient outward currents in single smooth muscle cells. *J. Gen. Physiol.* 113:215–228. http://dx.doi.org/10.1085/jgp.113.2.215

ZhuGe, R., K.E. Fogarty, S.P. Baker, J.G. McCarron, R.A. Tuft, L.M. Lifshitz, and J.V. Walsh Jr. 2004. Ca^{2+} spark sites in smooth muscle cells are numerous and differ in number of ryanodine receptors, large-conductance K^+ channels, and coupling ratio between them. *Am. J. Physiol. Cell Physiol.* 287:C1577–C1588. http://dx.doi.org/10.1152/ajpcell.00153.2004